January 2016

Light localization in biological media

Seung Ho Choi
Purdue University

Graduate School Form
30 Updated 12/26/2015

PURDUE UNIVERSITY
GRADUATE SCHOOL
Thesis/Dissertation Acceptance

This is to certify that the thesis/dissertation prepared

By Seung Ho Choi

Entitled
LIGHT LOCALIZATION IN BIOLOGICAL MEDIA

For the degree of Doctor of Philosophy

Is approved by the final examining committee:

Young L. Kim, Chair	Vladimir M. Shalaev
Bumsoo Han	Jenna Rickus

To the best of my knowledge and as understood by the student in the Thesis/Dissertation Agreement, Publication Delay, and Certification Disclaimer (Graduate School Form 32), this thesis/dissertation adheres to the provisions of Purdue University's "Policy of Integrity in Research" and the use of copyright material.

Approved by Major Professor(s): Young L. Kim

Approved by: George R. Wodicka 4/19/2016
Head of the Departmental Graduate Program Date

LIGHT LOCALIZATION IN BIOLOGICAL MEDIA

A Dissertation

Submitted to the Faculty

of

Purdue University

by

Seung Ho Choi

In Partial Fulfillment of the

Requirements for the Degree

of

Doctor of Philosophy

May 2016

Purdue University

West Lafayette, Indiana

To my wife Na Young and baby Jaewon

ACKNOWLEDGEMENTS

In the not too distance future: Corporate networks fill the Earth, electrons and light flow throughout the universe. Society, however, has not yet fully computerized to wipe out nations and ethnic groups. (Ghost in the Shell, 1995)

I deeply appreciate to my advisor Prof. Young L. Kim; committee members Prof. Bumsoo Han, Prof. Jenna Rickus, and Prof. Vladimir M. Shalaev; colleagues Dr. Azriel Genack (Queens College of the City University of New York), Dr. Wonshik Choi (Korea University), Dr. Hui Cao (Yale University), Dr. Johannes de Boer (University Amsterdam), Dr. Kyung Min Byun (Kyung Hee University), Dr. Kwang-Ho Choi (National Academy of Agricultural Science), Dr. Prabhakar Pradhan (University of Memphis), Dr. Tae-Won Goo (Dongguk University), Dr. Xiangeng Meng (Purdue University), Dr. Chia-Ping Huang (Purdue University), Dr. Christopher Gilpin (Purdue University), Dr. Zhou Shi (Queens College of the City University of New York), Dr. Sung Young Choi (Kyung Hee University), Dr. Sehoon Kim (Korea Institute of Science and Technology), Dr. Pan Chae Kim (Dongshin University), Dr. Chulmin Joo (Yonsei University), Dr. Jung Woo Leem (Purdue University), Richard Ajagu (Purdue University), Taehoon Kim (Purdue University), Zhuoxian Wang (Purdue University), John Rauchenstein (Purdue University), Siddhant Jaitpal (Purdue University), Nathan Lambert-Cheatham (Purdue University), and Michelle A. Visbal

Onufrak (Purdue University); and anonymous journal referees for participating journey to a space beyond unknowns.

TABLE OF CONTENTS

Page

Page

LIST OF TABLES

LIST OF FIGURES

Figure Page

ABSTRACT

Choi, Seung Ho. Ph.D., Purdue University, May 2016. Light Localization in Biological Media: Major Professor: Young L. Kim.

Light in natural and biological media is known as freely diffusing[1,2]. When light undergoes multiple scattering through inhomogeneous dielectric biomacromolecules, interference is ignored. If scattered waves return to their origin points along the time-reversed paths for constructive interference[3-5], outgoing waves can be forbidden, occasionally being on-resonance or off-resonance with Anderson localized modes[6,7]. However, such a phenomenon in optics requires high-refractive-index contrasts[8-11], which intrinsically do not exist in organic molecules (e.g. proteins, lipids, carbohydrates, and nucleic acids). Here we predict and show experimentally that the long-standing perception of diffusive nature of light in biological media is broken by an exquisite distribution of silk protein structures produced from *Bombyx mori* (silkworm) and layered aragonite structures produced from *Haliotis fulgens* (abalone). We demonstrate how optical transmission quantities (e.g. light flux in transmission channels) are analyzed satisfying critical values of the Anderson localization transition. We find that the size of modes is smaller than specimen sizes and that the statistics of modes, decomposed from excitation at the gain-loss equilibrium, clearly differentiates silk and

nacre from diffusive structures sharing the microscopic morphological similarity. This explains how the dimension, the size, and the distribution of disordered biological nanostructures result in enhanced light-matter interactions, in spite of low refractive index contrasts of constituent materials. As wave localization is universal, the presented results of electromagnetic waves will allow us to extend insight into electronic and mechanical waves in biological systems. Importantly, such optical resonances are extremely sensitive to subtle nanoscale perturbations, and thus can be implemented to biosensing platforms.

CHAPTER 1. LIGHT IN NATURAL SILK

1.1 Introduction

We find a clue from nature that possesses superior physical properties overcoming constituent material limitations. A silkworm secretes insoluble silk protein (i.e. fibroin) via numerous spigots of spinneret (i.e. silk spinning organ), which is crystallized to nanofibrils with air voids and is assembled into flat broad twin fibroin filaments[12] (Fig. 1b, c). A single silk filament with a size of $L \approx 20$ μm contains 3,800 nanofibrils (Fig. 1d). The Fourier transform of nanofibrillar images (Fig. 1e) shows the absence of periodicity, free from single spatial components (Fig. 1g). If each individual nanofibril serves as a scattering center and the scattered waves follow the time-reversal symmetry for constructive interference, Anderson localization could potentially be realized (Fig. 1a). Originally, Anderson localization describes the metal-insulator transition, resulting from scattering of the electronic wavefunction in random defects of the potential[13]. Although this concept is valid in a system where the total energy is conserved, this has recently been extended to systems with non-conservative bosonic fields (e.g. microwaves and light waves)[7,10,14]. The morphological characteristics inside a fibroin filament, obtained from post-processed TEM images (Extended Data Fig. 1) provide the clue for light

localization. The nearly parallel nanofibrils (Fig to be added), which lay along the longitudinal axis of the filament, can minimize the deviation of wave propagation from

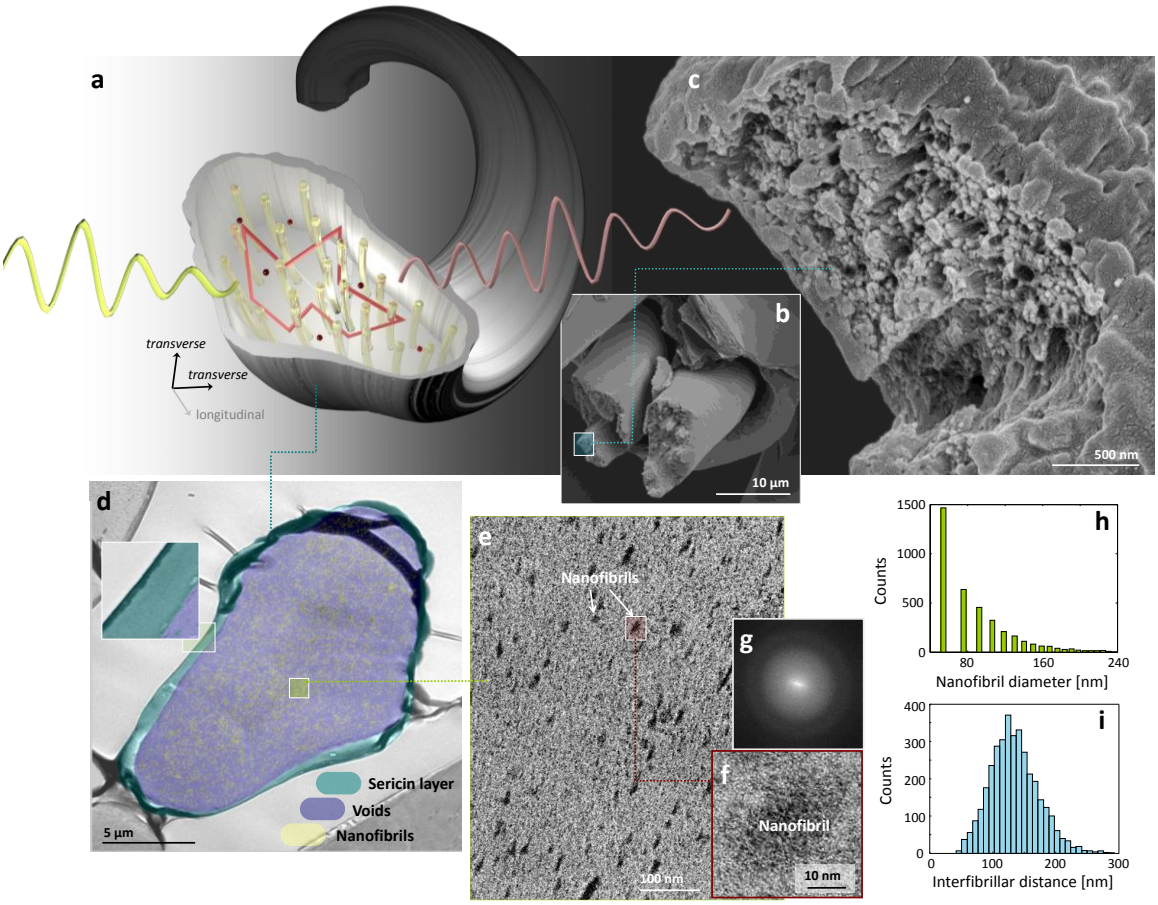

Fig. 1. Nanofibrillar structures in a silkworm silk filament.
a, Three dimensional (3D) illustration of light localization in a single silk filament of nanofibrillar structures (yellow translucent cylinders). **b**, **c**, SEM showing a fractured edge of fibroin filaments (**b**) and nanofibrils (**c**). **d**–**f**, TEM with different magnifications. The color-coded overlay in **d** distinguishes nanofibrils, voids, and sericin layers. The dark granule-like dots in **e** and **f** indicate nanofibrils. **g**, 2D fast Fourier transforms of **e**. **h**, **i**, Histograms of nanofibril sizes (**h**) and interfibrillar distances (**i**).

the transverse plane, in a manner analogous to light transport in 2D. Because of the reduced dimensionality, the waves can essentially be localized in the limit of $L \rightarrow \infty$[15-17]. The size distribution of nanofibrils D, ranging from 30 nm (Fig. 1f) to 200 nm (size

parameter $\pi D/\lambda \approx 1$ assuming λ = 600 nm and Fig. 1h), and the large number of scattering centers can enhance scattering power. The volume fraction of nanofibrils (~ 30% and Extended Data Fig. 1) is near an optimal value for avoiding scattering center overlaps[18]. Moreover, the distance between nanofibrils of 131 ± 37 nm (~ $\lambda/4$) (Fig. 1i) can maximize the wave interference, because the phase is accumulated by ~ $\pi/2$ in a silk filament. As the light propagates, the morphology of silk appears to be optimized for rapid phase randomization, which is vital for drastically decreasing the localization length of light ξ.

1.2 Results

1.2.1 Prediction of light localization

To understand the critical role of nanofibrils in light localization, we consider a structure directly from the TEM micrograph (Fig. 1d and Extended Data Fig. 1). Light waves within an area of a few filaments can appropriately be treated as 2D, due to the high degree of parallelism in nanofibrils (~to be added nm/mm) over a longitudinal distance of 10λ (Fig. 1j to be added), in spite of the microscopic twist appearance of fibers. In such a system, the observation of localization is challenged by an exponentially large ξ. For light confinement within an area over several micrometers, constituent scattering materials require high refractive indices $n > 2$[19], which are not available in living organisms; the highest-refractive-index biological material is guanine with n = 1.83[20]. However, using the finite element method (FEM) (Methods), we find that the energy is localized exponentially within a single filament possessing the natural distribution of nanofibrils

with $n_{\text{fibroin}} \approx 1.5 - 1.6$[21]. The confinement is evident from the high field intensity inside the filament (Fig. 2a) compared with the outside sericin layer and from the

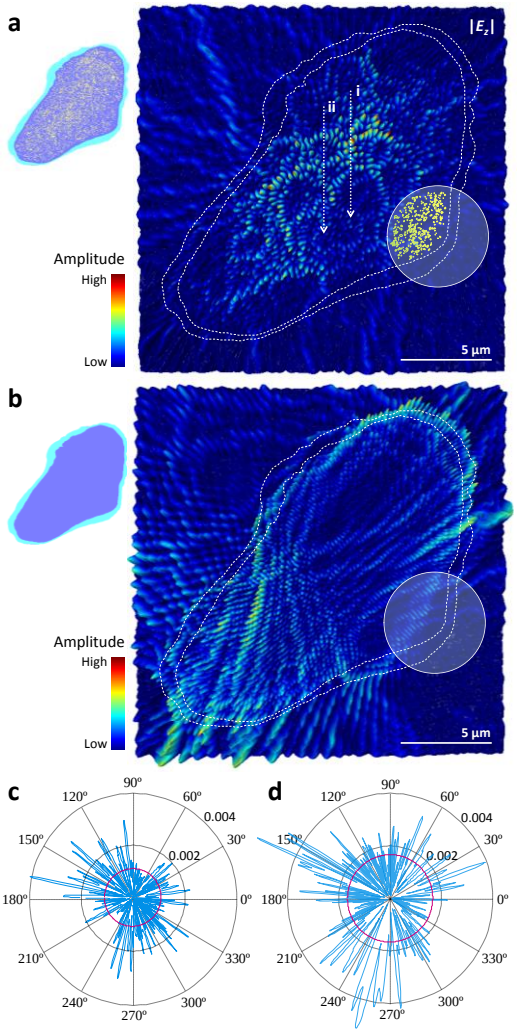

Fig. 2. Riddle of nanofibrils.
a, **b**, Electric field amplitude $|E_z|$ of modes in a single silk filament with **(a)** and without **(b)** nanofibrillar structures. The spreads of the fields along (i) and (ii) are 2.7 and 9 µm (Extended Data Fig. 4c, d). The overlays are the boundaries of sericin layers (white lines) and nanofibrils (yellow lines in insets) for computations. The boundaries and domains of nanofibrillar, interfibrillar, and sericin areas are extracted from high-resolution TEM micrographs (Extended Data Fig. 1). **c**, **d**, Far-field radiation patterns computed from the field of **a** and **b** using the near-to-far-field transformation, respectively. The red circles are average outgoing fluxes.

exponentially decaying envelopes at the center (Extended Data Fig. 4c, d). The local field width, which quantifies the degree of confinement (Supplementary Methods), is as narrow as 2.7 μm (Extended Data Fig. 4c). An average field width (~ 9 μm), which corresponds to 2ξ, is smaller than a single filament size. On the other hand, the waves in a bare silk filament without nanofibrils (Fig. 2b) are highly coupled to the free-space modes, inducing leaky resonances; its average outgoing flux is ~ 1.52 times higher than that of the nanofibrillar filament (Fig. 2c, d).

ξ is an intrinsic ensemble-averaged decay length of localized modes as a statistical property in a finite system. From 100 realizations of nanofibrillar structures, we calculate ξ = 4.5 μm (Extended Data Fig. 4a and Supplementary Methods), which is compatible to a measured mean free path length l = 3.5 μm (Extended Data Fig. 5 and Supplementary Methods). Interestingly, ξ is shorter than the average filament size $\xi < L$. Since the silkworm's spinning process stacks silk fibers, the thickness of the filament cluster (i.e. cocoon shell) significantly exceeds the localization length $L >> \xi$. Taking a cluster of filaments into account, different sets of nanofibrillar filaments, extracted from a TEM image, are systematically included in simulations. As more filaments (yellow lines in Fig. 3b and white lines in Fig. 3c) are added to surround the initial localization area (blue lines in Fig. 3a), the field intensity outside the cluster (i.e. leaking radiation) disappears progressively, indicating that the wave becomes deeply localized. The underlying scattering process is analyzed by decomposing the wave components in the modes as a function of wavevector k taking the Fourier transform of the field[17].

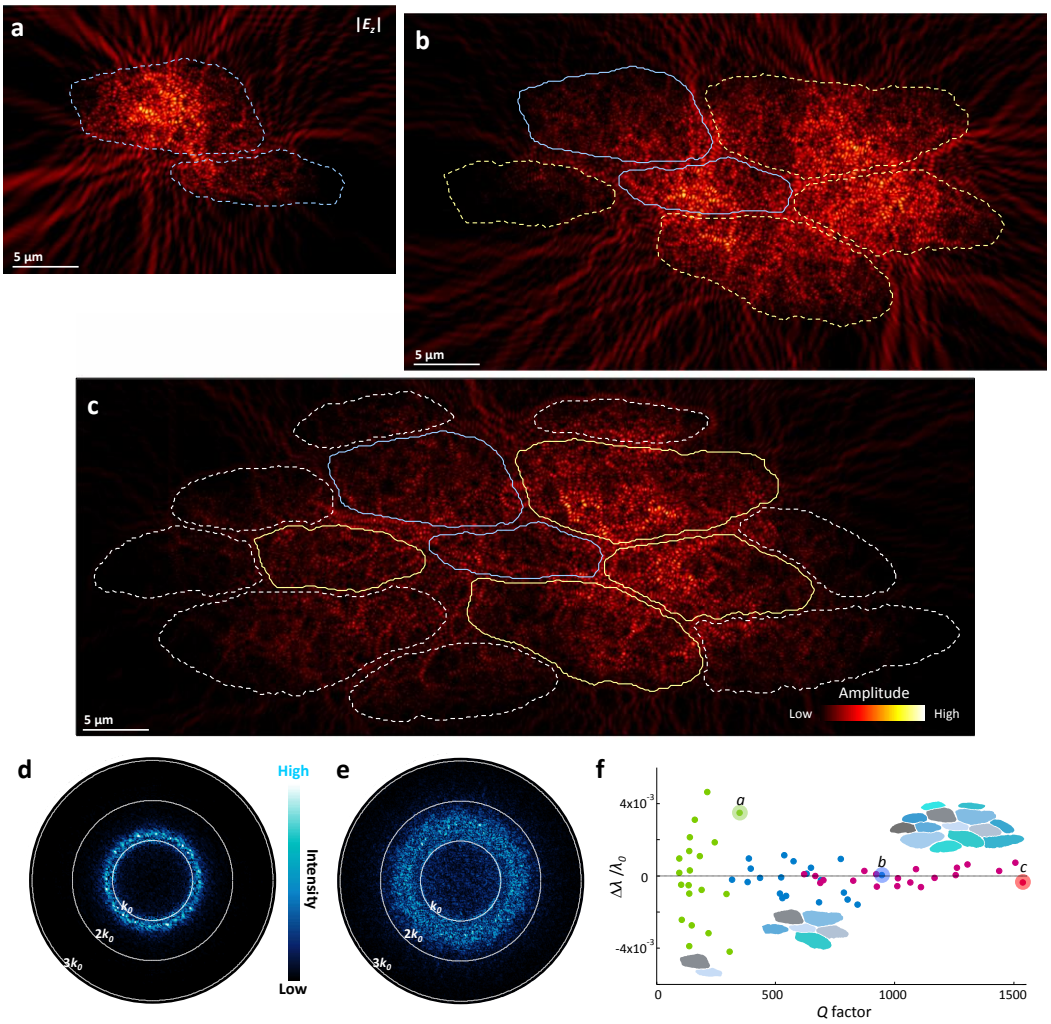

Fig. 3. Prediction of light localization.
a–**c**, Electric field amplitude $|E_z|$ of modes in two (**a**), six (**b**), and 14 (**c**) fibroin filaments with nanofibrillar structures at the wavelengths marked by the larger circles in **f**. The inner boundaries of sericin layers are marked by the colored lines. **d**, **e**, Norm of Fourier transform of the electric field E_z of **a** and **c**, respectively. **f**, Q factors of adjacent 20 modes around λ_0 = 600 nm. The green, blue, and red dots correspond to two-, six-, and 14-filament structures, respectively.

In Fig. 3d, e, rings in *k*-space show that the waves are scattered with their effective propagation constants in different directions. The ring thickness implies that the wave components are dispersed in *k*-space, due to interference among multiple scattering

paths. Compared to the two-filament cluster (Fig. 3d), the interference in the 14-filament cluster is more drastic (Fig. 3e), significantly dispersing the spatial components (*k*-vector) of the scattered waves and slowing down the propagation. Consequently, the mode is formed deep away from the boundary with negligible coupling to the free space. Indeed, the average quality *Q* factor in the 14-filament cluster has a 5.9-fold increase (Fig. 3f). The cooperation of multiple filaments also increases the mode density in wavelength (around λ_0 = 600 nm), which allows for effective confinement of broadband light (e.g. sunlight) in more wavelengths.

1.2.2 Interrogation of localization by external illumination

To characterize wave localization experimentally, we directly obtain *g* from transmission matrices (TM) (Fig. 4a and Methods). *g* is a fundamental localization parameter originally defined for the electronic wavefunction. For classical waves, the Landauer relation connects *g* to an ensemble average of the transmittance $< T >$ such that $g = < T > = \Sigma_{b,a} T_{ba} = \Sigma_a T_a$, where T_{ba} is the transmission intensity from an incident channel *a* into an outgoing channel *b* and $T_a = \Sigma_b T_{ba}$ is the total transmission[6,7,22]. When *g* falls below unity, Anderson localization results in sporadic resonance tunneling.

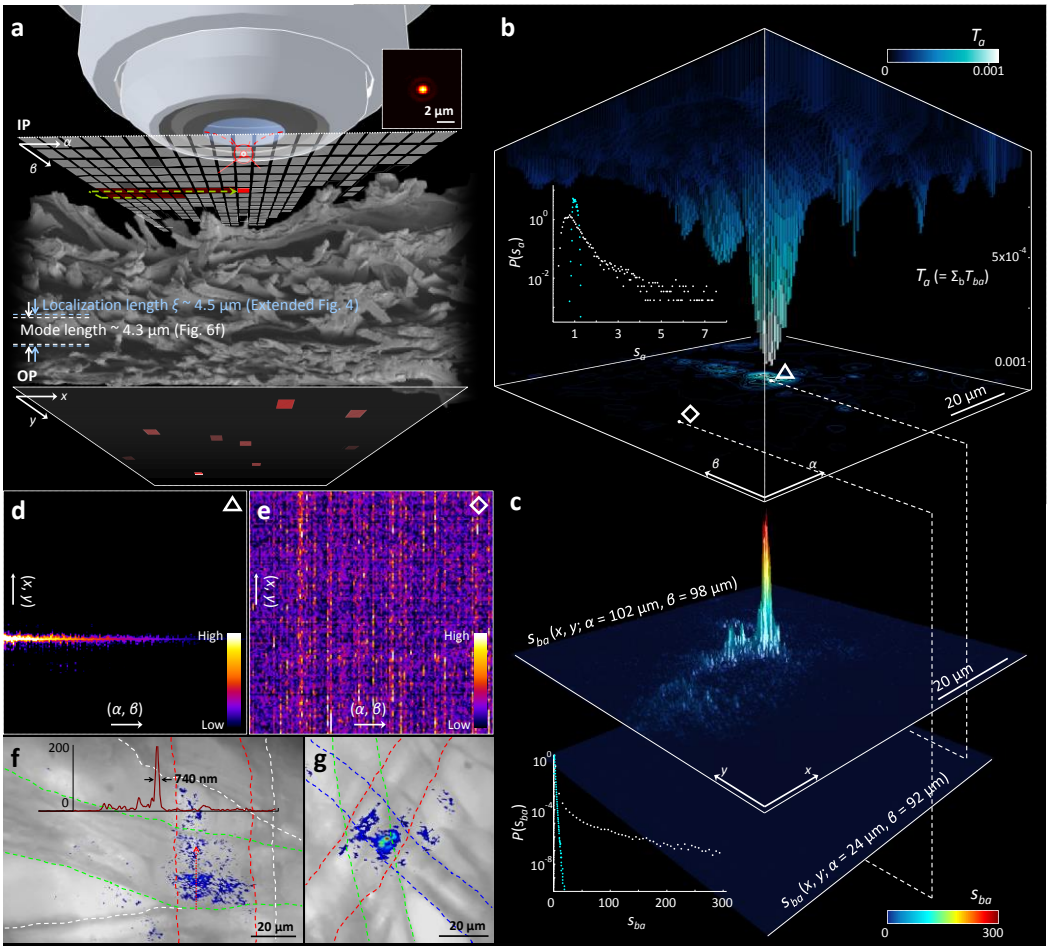

Fig. 4. Interrogation of localization by external illumination.
a, Schematic of optical transmission matrix (TM) measurements. External point-like illumination (inset: focal spot with a diameter ~ 1 μm) is scanned on the array of the input α-β plane (IP) and non-vanishing optical intensity through modes is imaged on the output x-y plane (OP). **b**, $T_a(\alpha, \beta)$ map of the silk cocoon. The bottom projection image visualizes a small number of transmissive channels. Inset: Probability distributions of s_a for the cocoon (white dots and var(s_a) = 0.5) and paper (cyan dots and var(s_a) = 5.2×10^{-3}). **c**, $s_{ba}(x, y)$ maps from two locations of Δ and ◊ in **b**. Inset: Probability distributions of s_{ba} from 10^4 translations of illumination for the cocoon (white dots) and paper (cyan dots) specimens. **d**, **e**, TMs from Δ and ◊ in **b**. Each column of TM is an arranged $T_{ba}(x, y)$ recorded at a position of (α, β). **f**, **g**, $s_{ba}(x, y)$ overlay (pseudo-color) on white-light microscopy images (grayscale) identifying mesoscopic fluctuations with a sharp field peak (FWHM ~ 740 nm), located on the stacks of multiple silk fibers (Extended Data Fig. 6). The boundaries of filaments are marked by the colored lines.

TM is obtained optically by measuring non-vanishing intensity patterns T_{ba} at the output plane (OP) (Fig. 4a). In the silk specimen, the light tends to scatter in the forward direction with an effective scattering angle $\vartheta \approx 39º$, which is obtained from the anisotropy factor $<\cos\vartheta> = 0.78$ (Supplementary Methods and Extended Data Fig. 5). Thus, the objective lenses (NA = 0.9) with the angular passband ($\sin^{-1}$(NA) = 64º) mostly collect the waves from the outgoing channels b of the specimen and effectively couple the input illumination into the incident channels a at the input plane (IP), in spite of a finite solid angle in optics (Methods). Mimicking the incidence of sunlight from free space onto the cocoon surface, a point-like source (λ = 632.8 nm) is illuminated on the surface of the specimen with an optical thickness of $L/l_t \approx 14$ (Supplementary Methods), resulting in T_{ba}. For TM, 10^4 images of T_{ba} is further assembled into a 100 × 100 array of $T_a(\alpha, \beta)$. Summing T_a for the all channels a, we obtain g = 1.4, which implies localization in silk proximal to the Anderson regime. This value is comparable with the state-of-art values of g, yet all of which were estimated from mesoscopic models; $g \approx$ 2.1 – 3.6 in 3D GaP nanowires[23] and $g \approx$ 0.6 – 5.6 in 2D ZnO nanoneedle arrays[24]. The significance of the silk's nanoarchitecture can be better understood, when we compare it with similar (on microscale) yet different (on nanoscale) synthetic systems. White paper is well known for its strong scattering with the appearance of whiteness, which has microstructures with bleached cellulose fibers coated by kaolinite or calcium carbonate[25]. Although the thickness of the paper specimen ($L/l_t \approx 14$ and Supplementary Methods) is optically comparable to the silk specimen, the light is highly diffusive as g = 128.5 (Methods and Extended Data Fig. 7).

To account for a potential decrease in g due to residual absorption, we determine localization in a complementary manner, using the variance of s_a (= $T_a/\langle T_a \rangle$)[6,7]; var(s_a) statistically measures the amount of fluctuations in a transmission quantity. In the entire area of $T_a(\alpha, \beta)$, the transport is dominated by the channel marked with Δ (Fig. 4b); T_a at Δ is significantly greater than $\langle T_a \rangle$. This results in a pronouncedly broad distribution function $P(s_a)$, deviating from a Gaussian distribution (inset in Fig. 4b)[26]. As a result, var(s_a) = 0.5 is close to the critical value of Anderson localization transition of 2/3[6,7]. The speckle pattern $s_{ba}(x, y)$ (= $T_{ba}/\langle T_{ba} \rangle$) through the channel Δ has a peak with a FWHM of 0.8 μm and a height of 300 (Fig. 4c). Such high fluctuations result in $P(s_{ba})$, deviating from a Rayleigh distribution (inset in Fig. 4c). For several inputs around Δ, the patterns of s_{ba} are surprisingly similar, giving rise to the horizontal bright line in the TM array (Fig. 4d), which occurs for localized waves[27]. In contrast, s_{ba} is weakly correlated for other positions of illumination where T_a is suppressed (◊ in Fig. 4e). Similarly to ◊, $s_{ba}(x, y)$ of paper is decorrelated, but in the entire IP (Extended Data Fig. 7c). The analyses of s_a and s_{ba} prove localization in white silk regardless of absorption, indicating light path crossing in the highly correlated speckle patterns[28] and illumination coupling with a limited number of localized modes. Such phenomena easily occur in cohesively bonded stacks of multiple silk fibers (Fig. 4f, g, and Extended Data Fig. 6).

1.2.3 Interrogation of localized modes by internal luminescence

To confirm the existence of localized modes inside the silk filaments, we excite cavities located far away from the sample surface using internal light sources and quantify them in multiple dimensions of space $\boldsymbol{r}$, frequency ω, and excitation energy E_{ex}. Embedding moderate gain (Extended Data Fig. 8) is particularly useful to examine the affluent phase space of localization without modifying the resonance properties of the underlying passive structures, because nonlinear effects of gain saturation and mode competition are nearly negligible for localized specimens[14,19,29,30]. At around the gain-loss equilibrium (i.e. lasing threshold), such a system compensates intrinsic loss and resembles a conservative medium (e.g. electronic conductors), in which the time-evolution operator is Hermitian. In this case, the electromagnetic emission can be expressed as a complete set of quasi-normal modes[7]:

$$I_m(\boldsymbol{r}, E_{ex}, \omega) = \sum_{h=1}^{H} a_h(\boldsymbol{r}, E_{ex}) \frac{\Gamma_h(\boldsymbol{r}, E_{ex})/2}{i(\omega - \omega_h(\boldsymbol{r}, E_{ex})) + \Gamma_h(\boldsymbol{r}, E_{ex})/2}, \quad (1)$$

where ω_h (= $2\pi c/\lambda_h$), Γ_h, and $a_h(\boldsymbol{r}, E_{ex})$ are the central frequency, the linewidth, and the intensity of hth mode in the space-energy domain $\boldsymbol{r}$-E_{ex}The set of unknowns (i.e. ω_h and Γ_h) are inversely estimated by fitting the mode expansion in equation (1) to measured spectra I_e in frequency (Fig. 5a and Extended Data Fig. 9 and 10). In $I_e(E_{ex}, \lambda)$, the decomposed modes have stable and non-interacting central wavelengths λ_h (Fig. 5b) and their intensity grows linearly one at a time (Fig. 5c). In Fig. 5b, raster scanning of the specimen at around the gain-loss equilibrium (= 3.5 μJ/pulse) creates a plethora of resonances in $I_e(\boldsymbol{r}, \lambda)$, which are confined spatially and separated spectrally (i.e. mode

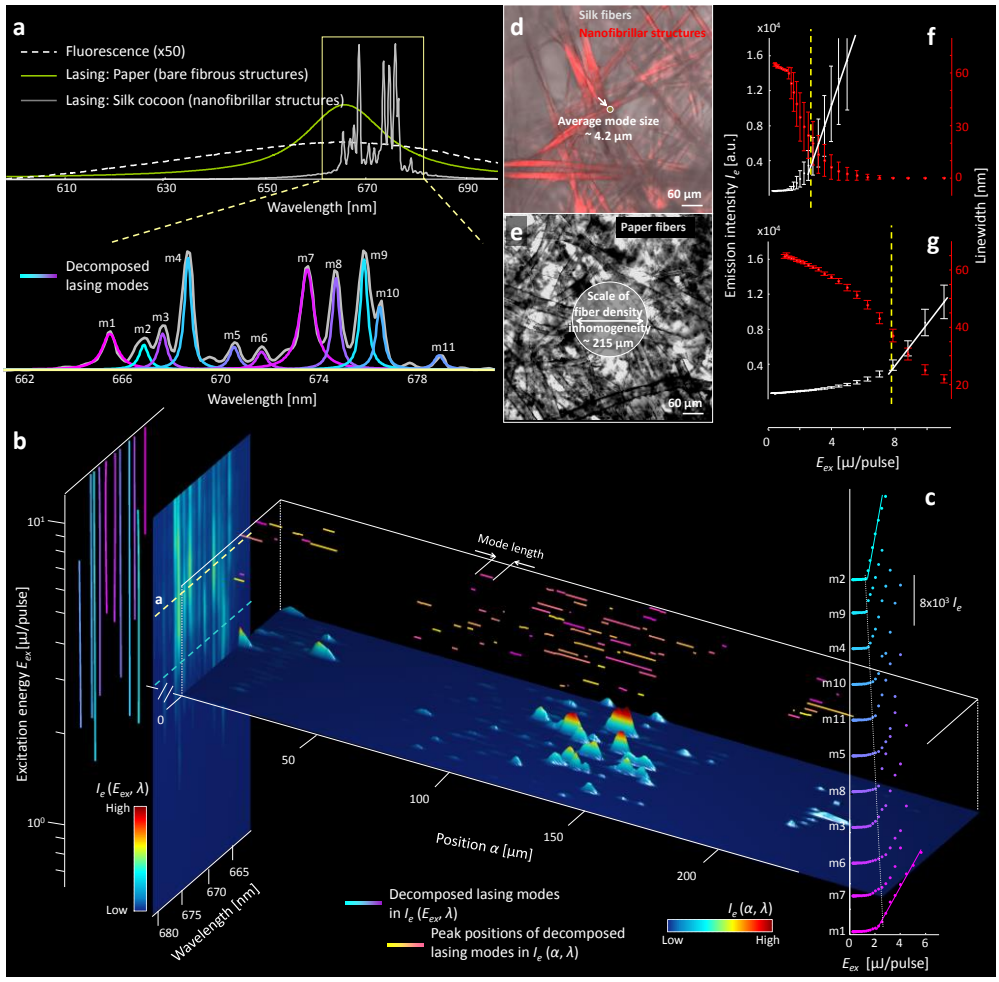

Fig. 5. Interrogation of localized modes by internal luminescence.
a, Modal decomposition (blue – magenta) of transmitted emission I_e (gray line) in **b** by inversely estimating a_h, ω_h, and Γ_h in the analytical expression of equation (1). The modes (m1 − m11) are color-coded with the thresholds plotted in **c**. **b**, Space-energy-wavelength spectrogram of emission $I_e(\boldsymbol{r}, E_{ex}, \lambda)$. Horizontal plane: $I_e(\boldsymbol{r}, \lambda)$ near the gain-loss equilibrium (= 3.5 μJ/pulse). $\boldsymbol{r}$ is the spatial coordinate on the input α-β plane. λ_h and Γ_h are clearly identified over the position α (on IP), where the mode intensity is greater than the baseline. The λ_h lines on the top (yellow − pink) delineate the spatial extent of modes. Vertical plane: $I_e(E_{ex}, \lambda)$. The λ_h lines on the left (blue − magenta) show suppression of modal interactions. **c**, a_h of single lasing modes decomposed in **a** as a function of E_{ex}. The blue and magenta colors indicate the lowest and the highest threshold. **d**, **e**, Average sizes of modes in silk (**d**) and spatial intensity fluctuations in paper (**e**), overlaid on optical microscopy images. **f**, **g**, Average intensity and linewidth of the decomposed lasing modes in silk (**f**) and the diffusive lasing peaks in paper (**g**) as a function of E_{ex}. The vertical yellow lines mark the average E_{ex}, corresponding to the system gain-loss equilibrium.

spacing ≥ linewidth). In the absence of nanofibrils, those sharp features disappear as observed in diffusive lasing (Fig. 5a and Extended Data Fig. 11). Clustering the modes that share the identical ω_h and Γ_h (marked with the same colors of yellow – pink in Fig. 5b), we obtain an average mode length (or spatial mode extent) of ~ 4.2 μm (Fig. 6f and Methods), which is in excellent agreement with the prediction of ξ = 4.5 μm. The suppressed modal interactions and the small mode volumes are the hallmarks of Anderson localization[14,30].

1.2.4 Statistical evidence on localization

We analyze the spatiotemporal properties of decomposed modes and their E_{ex} dependence, compared to the bare fibrous structures (i.e. paper). In the nanofibrillar structures (i.e. silk), the light is confined in an area smaller than a single filament (Fig. 5d and Fig. 6f), while being pronouncedly diffused in the absence of nanofibrils (Fig. 5e and Extended Data Fig. 11e, f). This small mode size in silk enhances the electromagnetic field and enables gain to compensate loss at low E_{ex}. Compared to the paper, the conversion efficiency (= dI_e/dE_{ex}) has a 4-fold increase and the lasing threshold has a 2.5-fold decrease (Fig. 5f, g and Fig. 6a−c). The asymmetric shape of the threshold distribution (Fig. 6c) implies that the light undergoes strong scattering[31]. Indeed, the Q factors (= ω_h/Γ_h) range from 2,000 to 8,000 (Fig. 6d), which are comparable to the values

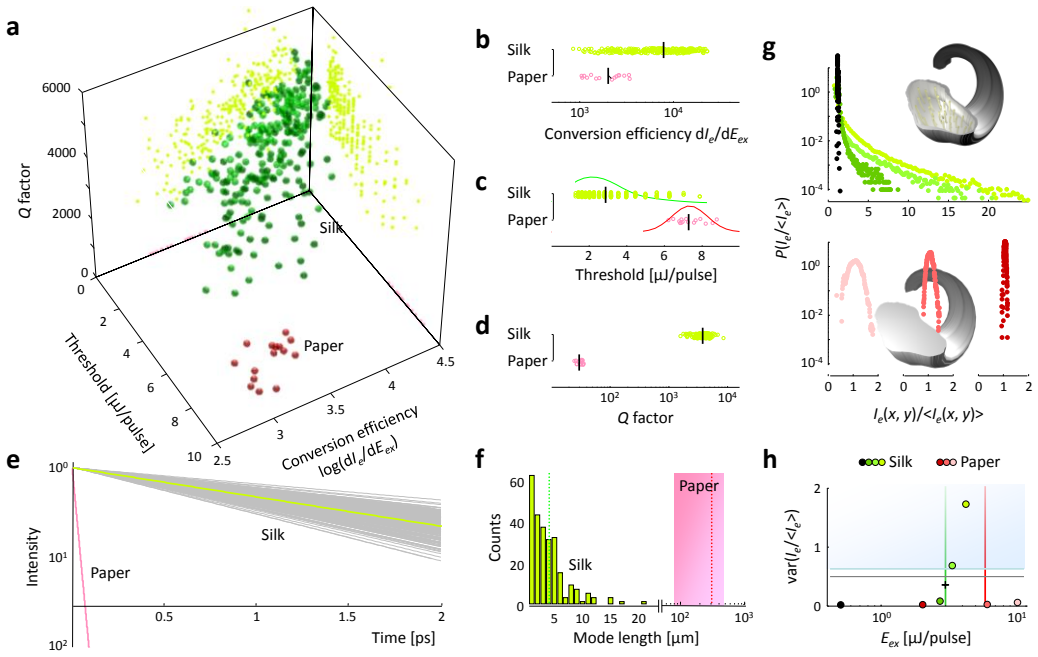

Fig. 6. Statistical evidence on localization.
a, *Q* factor, threshold, and conversion efficiency of decomposed modes. The *Q* factors are evaluated at the gain-loss equilibrium (Extended Data Fig. 10). The axial-plane projections show that the high *Q* factor modes have the enhanced lasing performance. The nanofibrillar structures (green dots) and the bare microfibrous structures (red dots) have the distinct properties of resonances and lasing. **b–d**, Pairwise comparisons of the distributions of the *Q* factor (**b**), the threshold (**c**), and the conversion efficacy (**d**) for silk and paper. **e**, Time-evolution of energy decay for the decomposed modes. The average decay rate of 1.38 ps^{-1} (green line) fundamentally corresponds to an average Γ_h = 0.11 THz. **f**, Mode lengths in silk determined from $I_e(\boldsymbol{r}, \lambda)$ (Methods). The red box marks a range of the spatial intensity fluctuations in paper. The dotted vertical lines mark their average sizes. **g**, $P(I_e/\langle I_e\rangle)$ for silk (top) and paper (bottom) at different E_{ex} that is color-coded in **h**. **h**, Degrees of localization captured by var($I_e/\langle I_e\rangle$) at different E_{ex}. The blue area indicates the Anderson localization regime above 2/3. The black line indicates var(s_a) of the passive systems (Fig. 4b). The + symbol marks var($I_e/\langle I_e\rangle$) at the lasing threshold in silk. The vertical lines are the average thresholds of each specimen (Fig. 5f, g).

from single quantized emitters in photonic crystal waveguides[32]. The *Q* factor is inversely proportional to the energy decay rate of the mode. The Fourier transform of the frequency variation term in equation (1) for $t > 0$ shows that the cavity storage time

of silk is ~ 130 times longer than that of bare fibers (Fig. 6e). Finally, we repeat statistical analyses for $P(I_e/\langle I_e \rangle)$. As E_{ex} increases, the system induces larger fluctuations in $I_e(\boldsymbol{r})$ as it recovers light confinement (Fig. 6g). The intensity variance $\mathrm{var}(I_e/\langle I_e \rangle)$ increases monotonically at around the threshold and surpasses > 2/3(Fig. 6h), which is the onset of Anderson localization[6,7]. We note that some modes are not loss-compensated and are damped at E_{ex} = 3.0 μJ/pulse (average threshold), resulting in slightly lower $\mathrm{var}(I_e/\langle I_e \rangle) \approx 0.4$ than that of the passive system (= 0.5 and Fig. 4b). The peculiarity of our observation is clear, compared to the Gaussian distributions from the typical fibrous microstructures even at high E_{ex} > 10 μJ/pulse. These results verify that we have observed Anderson-localized modes in silk near the gain-loss equilibrium, making fundamental differences in light-matter interactions, in which the two similar systems on the micron scale lack the topological similarity on the nanoscale.

1.3 Conclusions

Counterintuitively, we have shown that the phenotypic structures of silk produced by silkworms (*Bombyx mori*) bring their natural proteins into the regime proximal to the Anderson localization; this explains how silkworms have protected their pupae against photodamage[33] since the ancient times, while allowing small light transport for the life. The presented results will broaden our understanding of any linear wave phenomena in biological systems with strong interference, not just in optics (e.g. ultrasound and terahertz waves). Due to the high mode density in the visible range, the nanoarchitecture of silk fibers can be implemented to efficiently manage solar energy

for passive and scalable heating fabrics. In addition, silk is well known for the biocompatibility[21] and the preferable binding features to metal ions[34], making it potentially suitable for implantable resonators or imaging optical fibers [ref], and multifunctional smart textiles by hybridizing nanomaterials. An obvious next step would be to adopt a transverse localization scheme[16], in which illumination is coupled into the transverse dimension of a single silk fiber, so as to observe purely localized waves that stay after diffusive propagation, excluding leakage from the input.

1.4 Methods

1.4.1 Numerical experiments of modes using a finite element method (FEM)

The critical information on transport is carried in modes that can be obtained by solving the Hamiltonian of the system. To compute optical modes (also known as quasibound resonances) in a disordered media for light scattering problems, we considered a discretized Helmholtz equation that can be numerically solved by FEM[35]. For realistic simulations of a single silk filament as well as multiple filaments in a silk cocoon shell, we extracted the boundaries and domains of nanofibrils, interfibrillar areas, and sericin layers after post-processing high-resolution TEM micrographs (Extended Data Fig. 1a). Each silk fibroin filament typically contains $2\times10^3 – 6\times10^3$ nanofibrils, depending on the filament diameter. Thus, a series of large-scale electromagnetic simulations contained up to ~ 6×10^4 nanofibrils in 14-filament structures and generated ~ 10^7 triangular elements for FEM computations. The experimental values of refractive indices n of nanofibrils, interfibrillar areas, and sericin were 1.6, 1.0, and 1.34 at λ = 600 nm,

respectively[21]. For a uniform single silk fiber without nanofibrils, the refractive index of interfibrillar areas were set to be 1.6 to make zero refractive index contrast between the nanofibril and interfibrillar areas. The maximal mesh sizes were set to $\lambda/10$ in the interfibrillar areas and were reduced to $\lambda/20$ inside the nanofibrils due to their complex shapes (Extended Data Fig. 1d). For the boundary condition, a scattering boundary condition was applied on the surrounding rectangular computation domain up to 68 μm × 27 μm. Using RF Module of COMSOL Multiphysics (4.3a version), we computed all of the leaky modes near λ_0 = 600 nm for each disordered system and displayed the norm of E_z field component of the transverse magnetic (TM) mode. Each mode is represented by eigenfrequency κ, of which the real part Re(κ) is a resonant frequency and the imaginary part Im(κ) is associated with the width of resonance that determines the leaking radiation out of the system (i.e. loss). This yields the quality Q factor defined as $Q = -\text{Re}(\kappa)/2\text{Im}(\kappa)$. The field of the modes was analyzed to characterize the angular leaking radiation intensity (Fig. 2c, d) and to decompose wave components as a function of wavevector $k = 2\pi/\lambda$ (Fig. 3d, e).

1.4.2 Optical measurements of transmission matrices (TMs)

To characterize light localization in white silk cocoons, the inner compartment of a native silk cocoon (L = 220 μm) was used as experimental specimens, because the fiber distribution is more uniform than that the outer compartment (Extended Data Fig. 3c). As shown in Fig. 4a, we obtained TMs by imaging optical speckle patterns T_{ba} through the specimen at the output plane (OP) (x, y) using a microscopy imaging setup[23,39,40]. A

collimated beam from a HeNe laser (λ = 632.8 nm) was focused on the input plane (IP) with a FWHM of ~ 1 μm (inset of Fig. 4a) via an objective lens with NA = 0.9 (Meiji MA970 Plan Achromatic) for point-like illumination. The transmission intensity at the output plane (OP) was collected via another objective lens with NA = 0.9 (Meiji MA970 Plan Achromatic) and was imaged using a four-megapixel interline monochrome CCD camera. In the silk specimen, the light tends to scatter in the forward direction with an effective scattering angle of $\cos^{-1}(0.78) = 39º$ (Extended Data Fig. 5 and Supplementary Methods). Thus, the objective lenses, which have an angular passband of $\sin^{-1}(\text{NA}) = 64º$, mostly collect the waves from the outgoing channels b of the specimen and effectively couple the input illumination into the incident channels a, in spite of a finite solid angle in optics (Methods). The point-like illumination was scanned on channels at the transverse dimension of the incident plane (IP) (α, β), by moving the specimen mounted on a two-axis motorized micropositioner (Zaber T-LSR150A). Taking the full width of illumination (~2 μm) into account, the unit translation step in (α, β) positions was set to 2 μm to avoid overlapping illumination between adjacent positions. For each TM, 10^4 images of T_{ba} were acquired by translating the specimen in an area of 200 μm × 200 μm, which results in a 100 × 100 array of T_a. TM provides a full account of the input-output responses[22,36,37] (i.e. T_{ba}, T_a, and T) and the statistics of their normalizations (i.e. $s_a = T_a/\langle T_a \rangle$ and $s_{ba} = T_{ba}/\langle T_{ba} \rangle$), making it possible to directly assess g in a single system. To minimize the effect of the background intensity on statistical analyses of $P(s_{ba})$ and $P(s_a)$, we used image areas defined by a half maximum of the ensemble averaged image. Distributions of s_{ba} and s_a were compared with diffusive specimens of

white paper (L = 100 μm, $L/l_t \approx 14$, $\langle \cos \vartheta \rangle = 0.1$, and Extended Data Fig. 5b), which also has fibrous microstructures (Extended Data Fig. 7).

1.4.3 Measurements of $I_e(\boldsymbol{r}, E_{ex}, \lambda)$ and analyses of localized modes

To probe localized modes in white silk cocoon shells, we embedded luminescence sources to couple into the internal cavities, which are transferred to far-field radiation patterns near the gain-loss equilibrium. In sericin-removed silk filaments[38] (Supplementary Methods), the 3D volume of nanofibrillar structures is uniformly infiltrated by DCM in dimethyl sulfoxide (low reabsorption and quantum yield = 75%) at a low concentration of 0.5 mg/ml (Extended Data Fig. 8). An excitation beam from a frequency-doubled Q-switched Nd:YAG laser (pulse duration of 400 ps, repetition rate of 5 Hz, and λ of 532 nm) was focused on the specimen with a FWHM of ~ 1.8 μm via an objective lens with NA = 0.4[39,4042,43]. $I_e(\boldsymbol{r}, E_{ex}, \lambda)$ was collected via the same objective lens used in the TM setup and was detected by a spectrometer with a spectral resolution of ~ 0.15 nm, while scanning the specimen with a unit translation step of 500 nm and controlling E_{ex} using a continuous variable linear neutral density filter. For simultaneous modal decomposition, we searched ω_h, Γ_h, and a_h that minimize the sum of squared differences between equation (1) and measured spectra I_e, using the Nelder-Mead simplex method[41,42]:

$$\min \quad F = \sqrt{\frac{1}{S}\sum_{s=1}^{S} \left\| I_e(\omega_s) - I_m(\omega_s, a_h, \omega_h, \Gamma_k) \right\|^2}, \qquad (2)$$

where F is the objective function to be minimized, //…// is the Euclidian norm, and S is the number of points within the frequency of interest. An average number of modes per certain $\boldsymbol{r}$ and E_{ex} is H = 12 with 36 unknowns. In such multivariate optimization, because the iterative solutions can be trapped in local minima or can be diverged, the algorithm was set to contain multiple groups of initial guesses[41,42]. An example of fitted maps $I_m(E_{ex}, \lambda)$ is shown in Extended Data Fig. 9 and the full results of decompositions (i.e. a_h, ω_h, and Γ_h) are visualized in Extended Data Fig. 10a–c. We evaluated the Q factors (= ω_h/Γ_h) at the threshold of each decomposed mode. In $I_e(\boldsymbol{r}, \lambda)$, the mode length l_m was obtained:

$$l_m = \frac{\int \varepsilon(r) I_m(r) dr}{\varepsilon(r_0) I_m(r_0)}, \quad (3)$$

where $I_m(r)$ is the spatial emission profile of the decomposed mode sharing the same ω_h and Γ_h, ε is the dielectric constant, and r_0 is the anti-node position of the mode. Finally, single-shot measurements over 300 successive excitation pulses verified the temporal stability of lasing spectra used for the current mode analyses (Extended Data Fig. 10d, e).

1.5 Extended Data Figures and Figure Captions

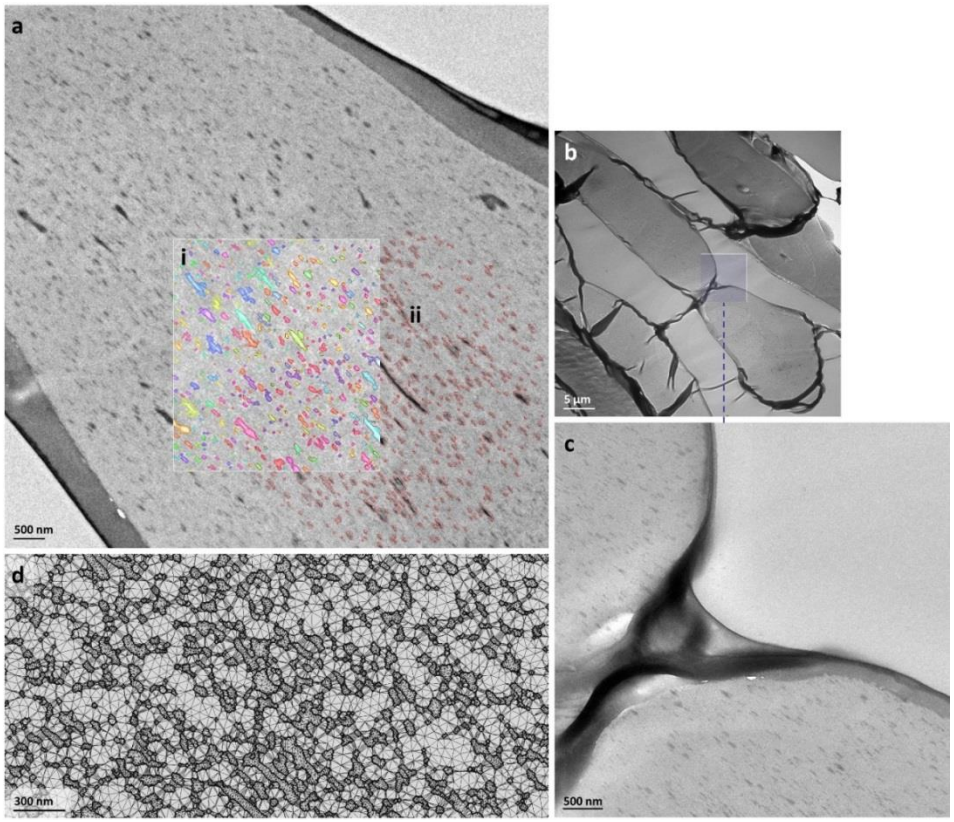

Extended Data Fig. 1. Post-processing of TEM images to extract nanofibrillar boundaries and domains for FEM computations.
a, Extraction of the boundaries and domains of nanofibrils, interfibrillar areas, and sericin from TEM micrographs for FEM computations. The dark granule-like dots indicate nanofibrils resulting from higher electron density of metal-stained nanofibrils than that of voids. The non-uniform background intensity in the filament is estimated using a morphological opening algorithm and is subtracted from the raw image. Then, a binary image is generated by increasing its image contrast and applying a threshold. From the binary image, connected components are identified, marked as the different pseudo-colors in (i). Using the connected components, the region boundaries are traced with the red lines in (ii). The volume fraction of nanofibrils is ~ 30%, which is defined as a fraction of the area occupied by the nanofibrils to the total area of the binary image. **b**, TEM micrograph of the transverse cross-section of two fibroin filaments in the silk fiber. **c,** Higher magnification TEM micrograph from the area marked by the rectangular box in **b** shows the presence of nanofibrils (dark granule-like dots) inside the fibroin filament and the absence outside the sericin layer. **d,** Representative boundaries and triangular meshes used in FEM computations. The thick black lines represent the boundaries of nanofibrils. The maximal mesh sizes are set to $\lambda/10$ in the interfibrillar areas and are reduced to $\lambda/20$ inside the nanofibrils, due to their complex shapes.

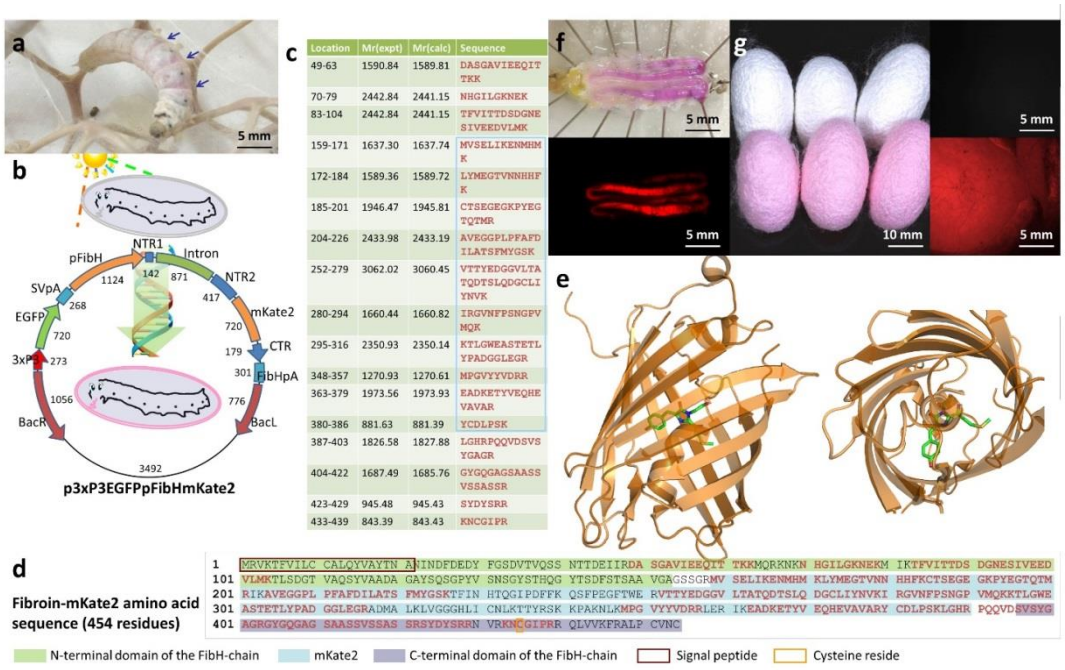

Extended Data Fig. 2. Silkworm transgenesis for molecular imaging of nanofibrils. **a**, Photograph of a transgenic silkworm in the rearing environment. The color of FibH chain-mKate2 fusion proteins (arrows) appears beneath the epidermis. **b**, Physical map of the transformation vector of p3xP3-EGFP-pFibH-mKate2. **c**, Identification of FibH chain-mKate2 fusion proteins by high-performance liquid chromatography with tandem mass spectrometry (LC-MS/MS). *De novo* sequences of tryptic fragments Mr(expt) are confirmed to match with the deduced amino acid sequences of FibH chain-mKate2 fusion proteins Mr(calc). **d**, Amino acid sequences of FibH chain-mKate2 fusion proteins. **e**, Stereoview of the chromophore (green sticks) in the crystal structure of mKate2 at a physiological pH of 7.5, visualized by using PyMOL (PDB: 3SVR). mKate2 is a S158A variant of mKate that replaces Ser^{158} of mKate by a hydrophobic residue, causing partial destabilization of the dimmer *trans* state of chromophore. This induces the equilibrium toward the brighter *cis* state (green sticks), thus being more pH-stable and increasing the brightness at a physiological pH. **f**, Photograph (upper) and fluorescent image (lower) of the silk gland of the larva on the 3^{rd} day of the 5^{th} instar. **g**, Photograph of the white (upper) and fluorescent (lower) silk cocoons produced by wild-type and mKate2-expressing silkworms and corresponding fluorescent images.

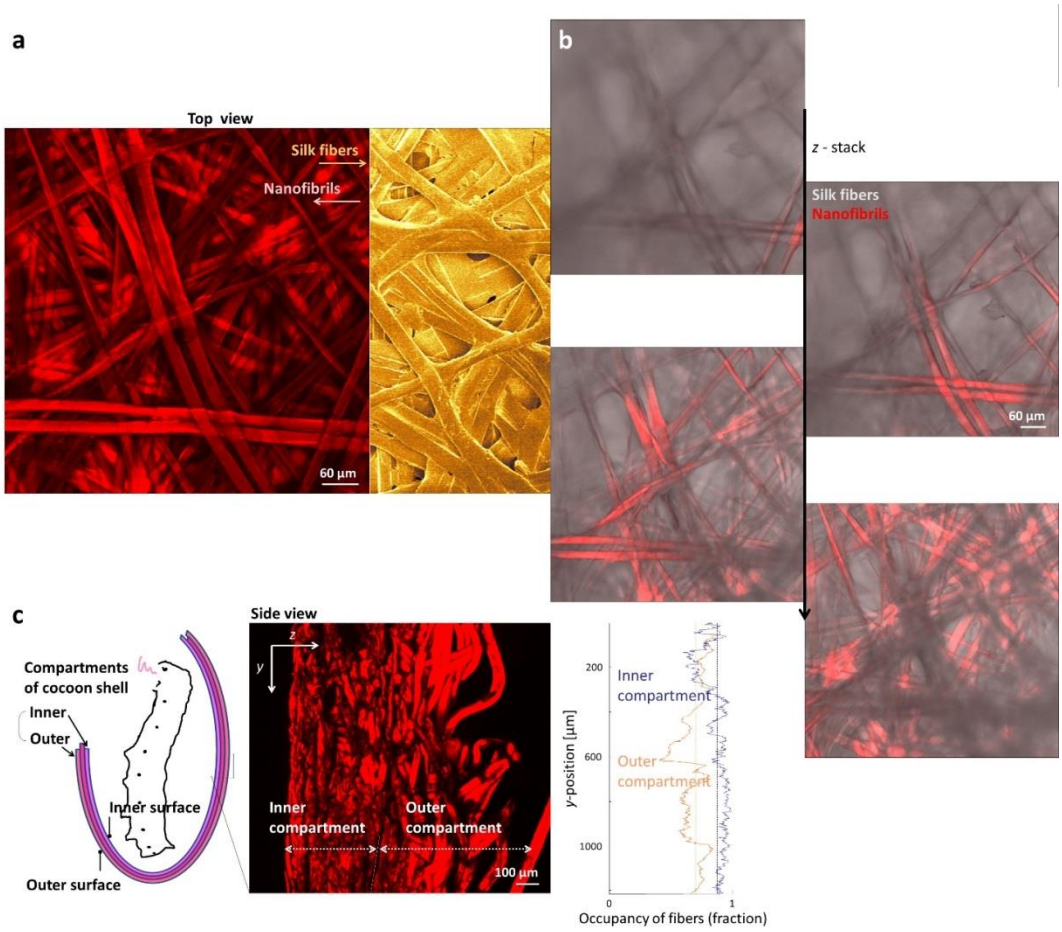

Extended Data Fig. 3. Molecular imaging of nanofibrils, showing the distribution of nanofibrils on microscales.

a, Left: Confocal fluorescence microscopy image of mKate2-expressing silk nanofibrils. Right: SEM image of the silk fiber surfaces. **b**, Serial optical sections with a step size of 14 µm. Reflectance (gray) and fluorescence (red) microscopy images are overlaid. The nanofibrils cover the whole area of the silk cocoon, forming the highly packed multilayered microstructures. **c**, Cross-section of the silk cocoon. Left: Compartments of the cocoon shell. Middle: Confocal fluorescence microscopy image of the cross-section. Right: Occupancy of silk fibers over *z*-axis. The fibrils of the inner compartment are more uniformly and highly packed than those of the outer compartment. Thus, the inner compartment of native silk cocoons is used for optical measurements (Fig. 4 and 5).

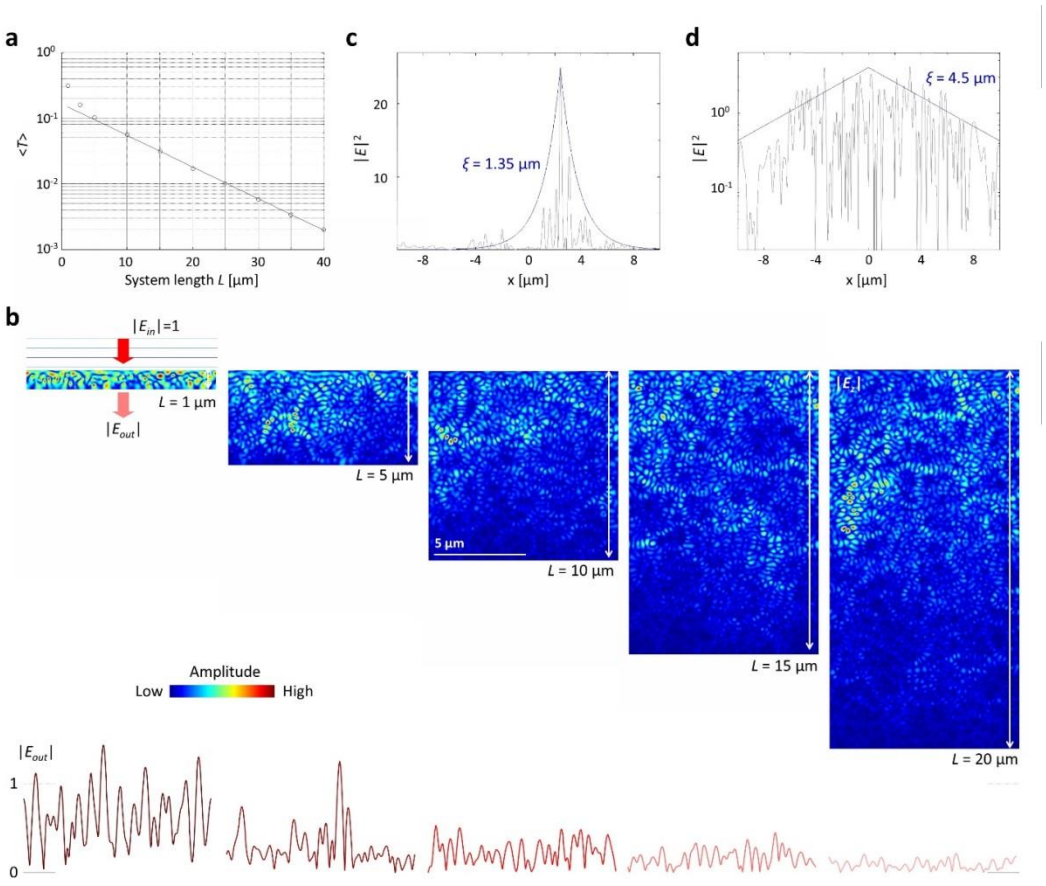

Extended Data Fig. 4. Calculations of the localization length of light ξ.
a, Computed average transmittance $< T >$ through the nanofibrillar system (representative domains are shown in Fig. 1d and Extended Data Fig. 1a). For a large system length of $L > 5$ μm, the decay over L converges to a single exponential and fitting a slope of $< \ln T > \approx -L/2\xi$ carries out $\xi = 4.5$ μm. **b**, Computations of plane wave propagation using FEM, through the nanofibrillar system of $L = 1$, 5, 10, 15, and 20 μm. The plane wave at $\lambda = 600$ nm with unit amplitude is launched at the top plane. The transmitted amplitude patterns $|E_{out}|$ at the output plane are shown by the red curves (bottom). For visual clarity, the amplitude is displayed rather than the intensity. **c**, **d**, Field intensity profiles along the white lines marked by i (**c**) and ii (**d**) in Fig. 2a. The blue curves are obtained by Eq. S3 with the estimation of ξ from an inverse participation ratio (Eq. S2).

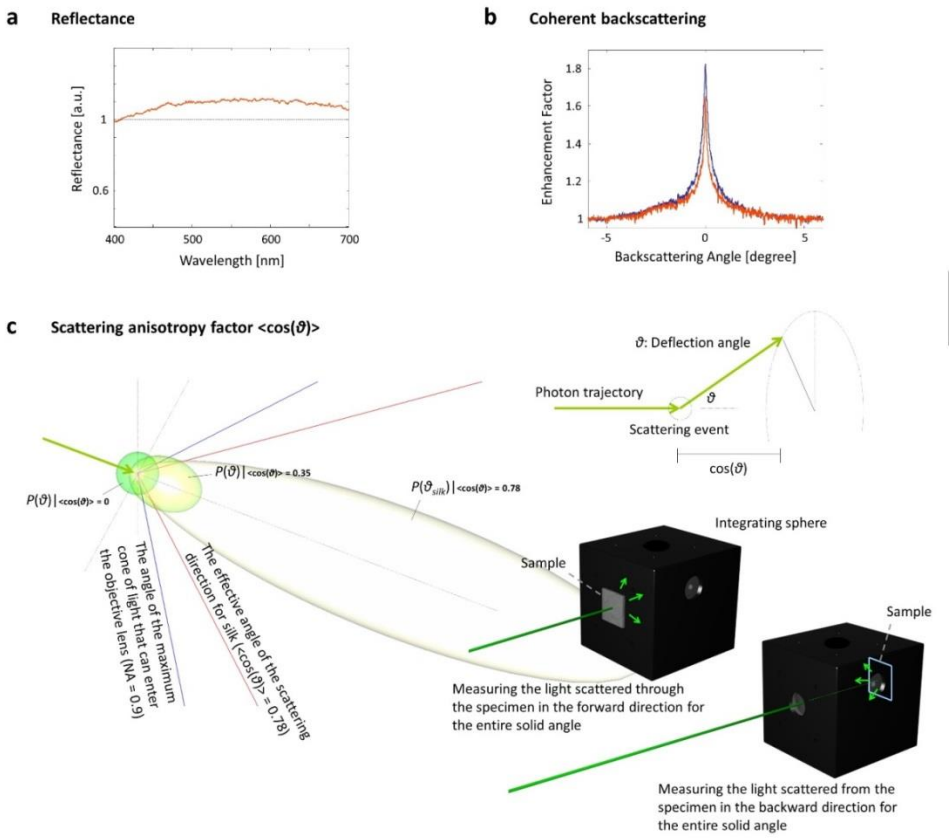

Extended Data Fig. 5. Measurements of the scattering mean free path length of light l_s and the scattering anisotropy factor <cosϑ>.
a, Average reflectance spectrum from a white silk cocoon: Reflectance spectra are obtained in the backward direction (within a small angular cone of ± 2°) and are averaged from 350 different spatial positions with a spatial binning size of 50 µm. The high and relatively flat reflectance over a broad spectrum indicates that the silk structure is optically dense with negligible absorption in the ultraviolet-visible range. The black dotted line is a reference reflectance obtained from a white reflectance standard with a reflectivity of 99% (Labsphere SRS-99-010). **b**, Measurements of the transport mean free path length l_t from coherent backscattering of light. A beam with a diameter of 3 mm from a He-Ne laser at 543.5 nm is illuminated onto the specimen on a rotating stage. The angular profiles of coherent backscattering carry out l_t = 16 µm and 7.3 µm for the white silk cocoon (red curve) and white paper (blue curve) specimens, respectively. **c**, Measurements of the scattering anisotropy factor <cosϑ> using an integrating sphere. Top right: Deflection of light trajectory by elastic scattering at ϑ. Bottom right: Schematics of forward and backward scattering measurements for entire Ω. Followed by measurements of the specimen, the standard, and the background, the inverse adding-doubling computations return <cosϑ> = 0.78. Left: 3D surface plots of the probability density of scattering as a function of ϑ, approximated by the Henyey-Greenstein phase function (Eq. S7) when <cosϑ> = 0, 0.35, and 0.78.

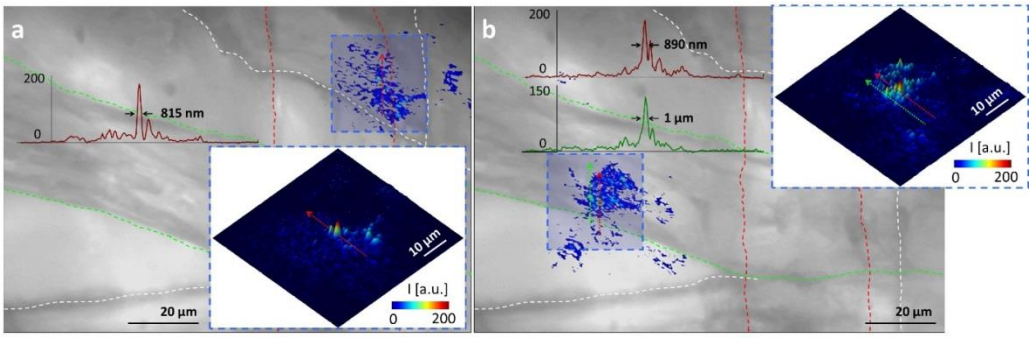

Extended Data Fig. 6. Extra tunneling locations in Fig. 4f.
a, **b**, Resonance tunneling occurs on the stacks of filaments marked by white (**a**) and green (**b**) boundaries. The transmission is near zero for other locations of the input illumination in the field of view of Fig. 4f. The background (grayscale image) is a microscopy image of the surface of the silk cocoon obtained by incoherent white-light large-area illumination. The speckle images ($s_{ba}(x, y)$ maps in pseudo-color) and the grayscale image are taken on the same focal plane of the most outer surface of the silk fibers. Insets: The surface plots of $s_{ba}(x, y)$ from the areas marked by the blue-shaded boxes and the cross-sections at their highest peaks (along the colored arrows on the surface plots) for visual clarity.

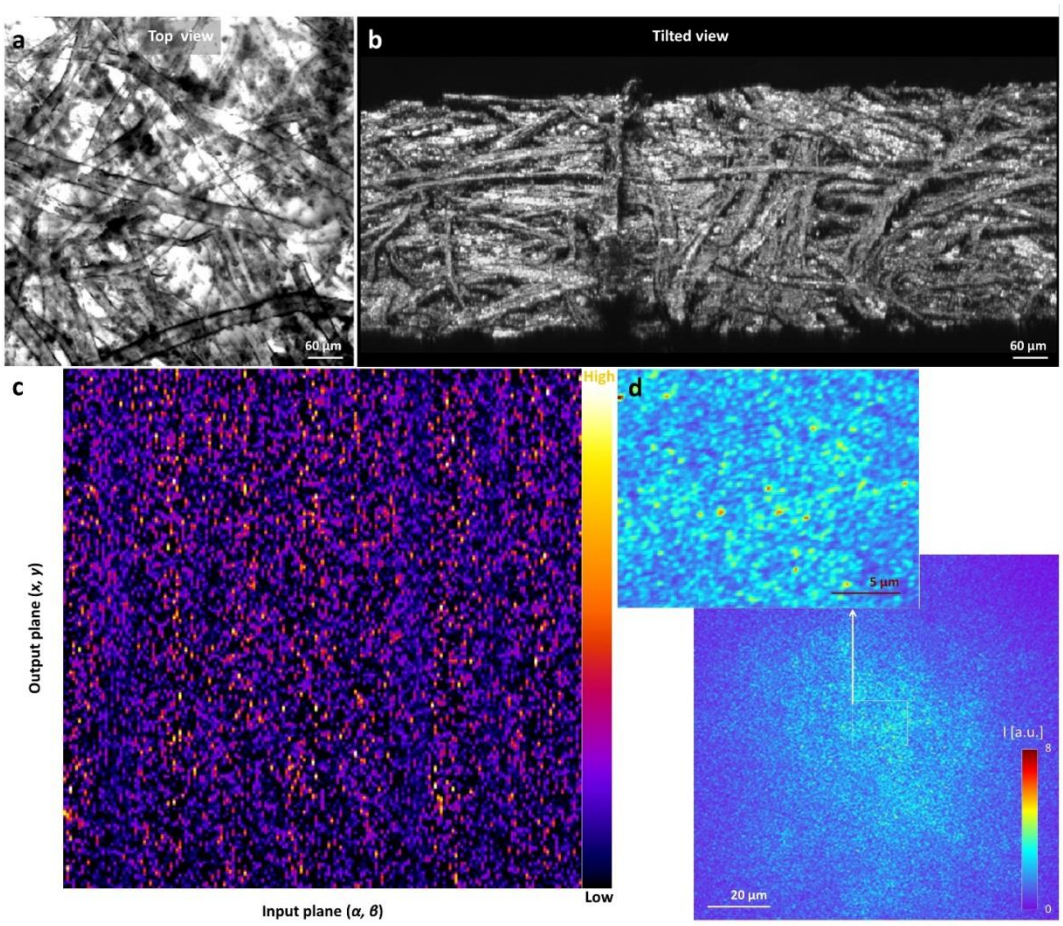

Extended Data Fig. 7. Disappearance of light localization when fibers lose nanofibrils. **a, b,** Reflectance confocal microscopy images of the white paper specimen in top (**a**) and tilted (**b**) views. **c,** TM of the white paper specimen after removing the fluctuation components originated from the background local sample inhomogeneity. Each column of TM is an arranged $T_{ba}(x, y)$ recorded at a position of (α, β). **d,** Representative $s_{ba}(x, y)$ maps. The uniformity of speckle patterns is captured as a Rayleigh distribution in $P(s_{ba})$ in the inset of Fig. 4c. The waves are diffusive as predicted in Fig. 2b.

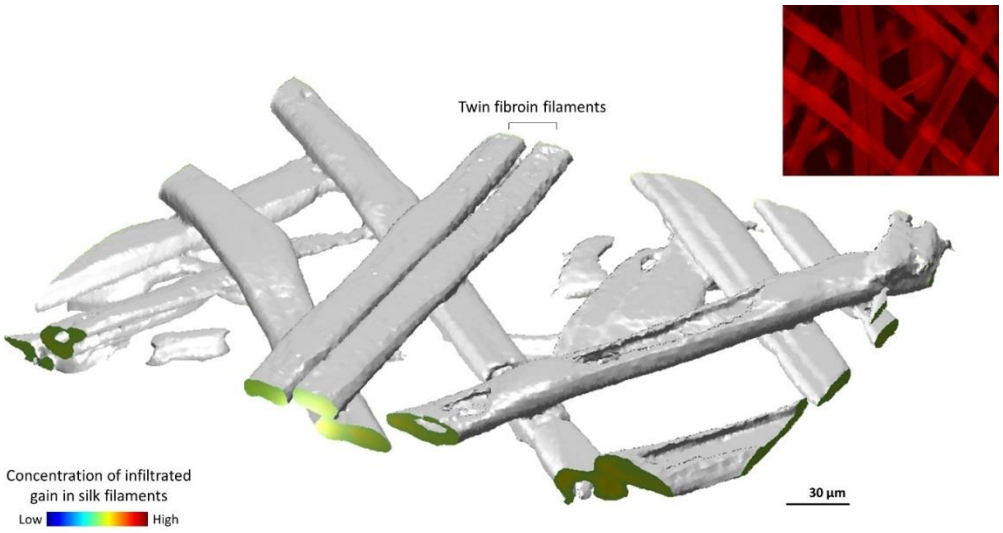

Extended Data Fig. 8. Internal luminescence embedded in silk filaments.
3D rendering of silk fibroin filaments infiltrated with DCM. The isosurface (gray color) represents a level set of gain concentrations in the reconstructed volume. The cross-sections (pseudo-color map) show the homogenous distribution of gain, allowing for compensating system loss and characterizing modes inside the filaments. The reconstructed 3D concentration of gain is obtained by a *z*-stack of confocal fluorescence microscopy images (top right: 2D projection of images over the *z*-axis).

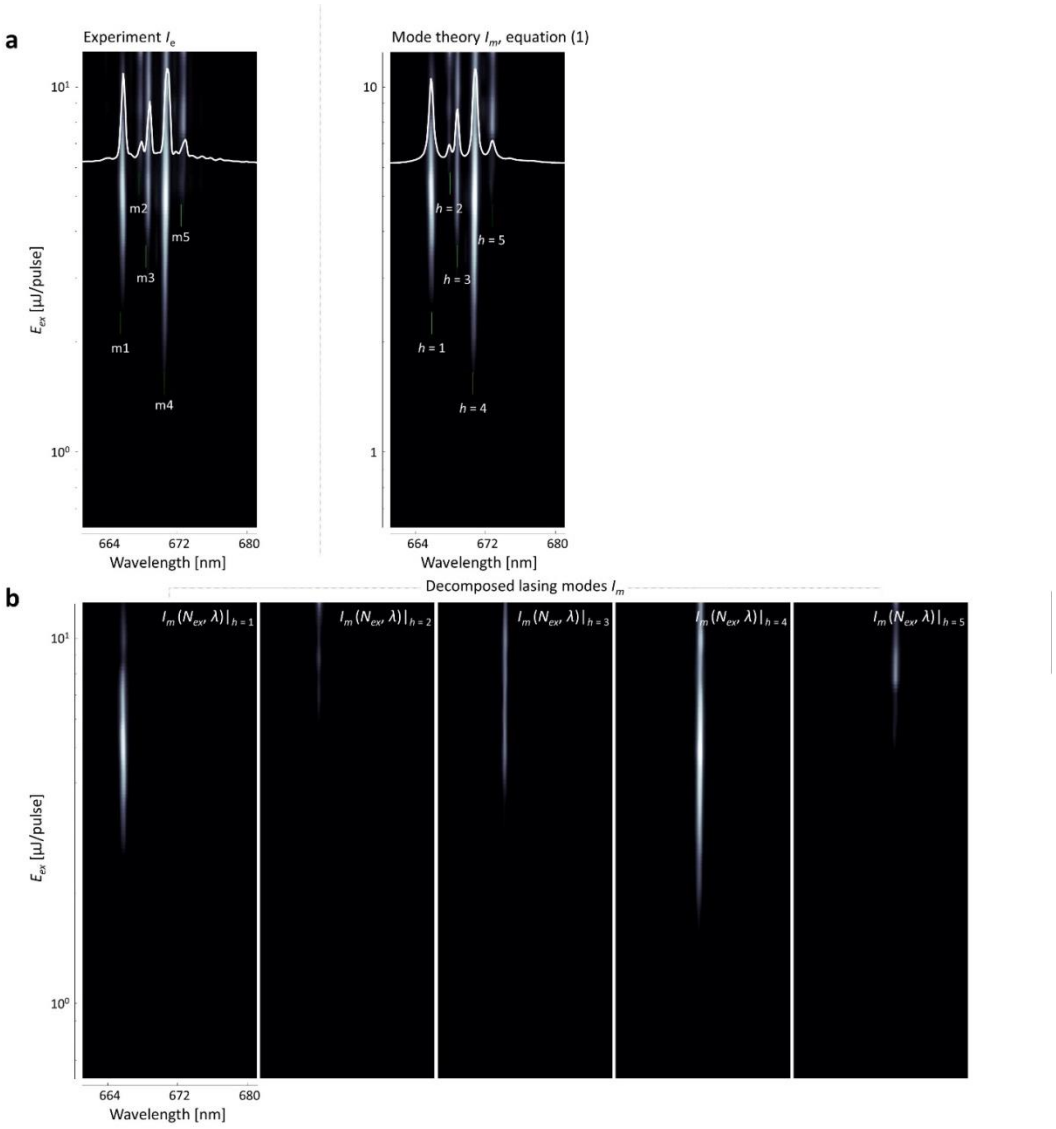

Extended Data Fig. 9. Modal decompositions of $I_e(E_{ex}, \lambda)$.
a, Left: Measured $I_e(E_{ex}, \lambda)$ from the silk cocoon shell. The spectra show five non-interacting lasing peaks marked with m1 – m5. Right: Spectra obtained by substituting the inverse estimations of a_k, ω_k, and Γ_k to the analytical expression of equation (1) ($I_m(E_{ex}, \lambda)$ with a total number of modes of $H = 5$). The representative cross-sections at E_{ex} = 6.2 μJ/pulse (white lines) are plotted for comparison between the fitted and measured spectra. **b**, Spectral evolution of decomposed single lasing modes as a function of E_{ex}. Five lasing modes have their consistent central wavelengths λ_h, while each shows threshold behavior.

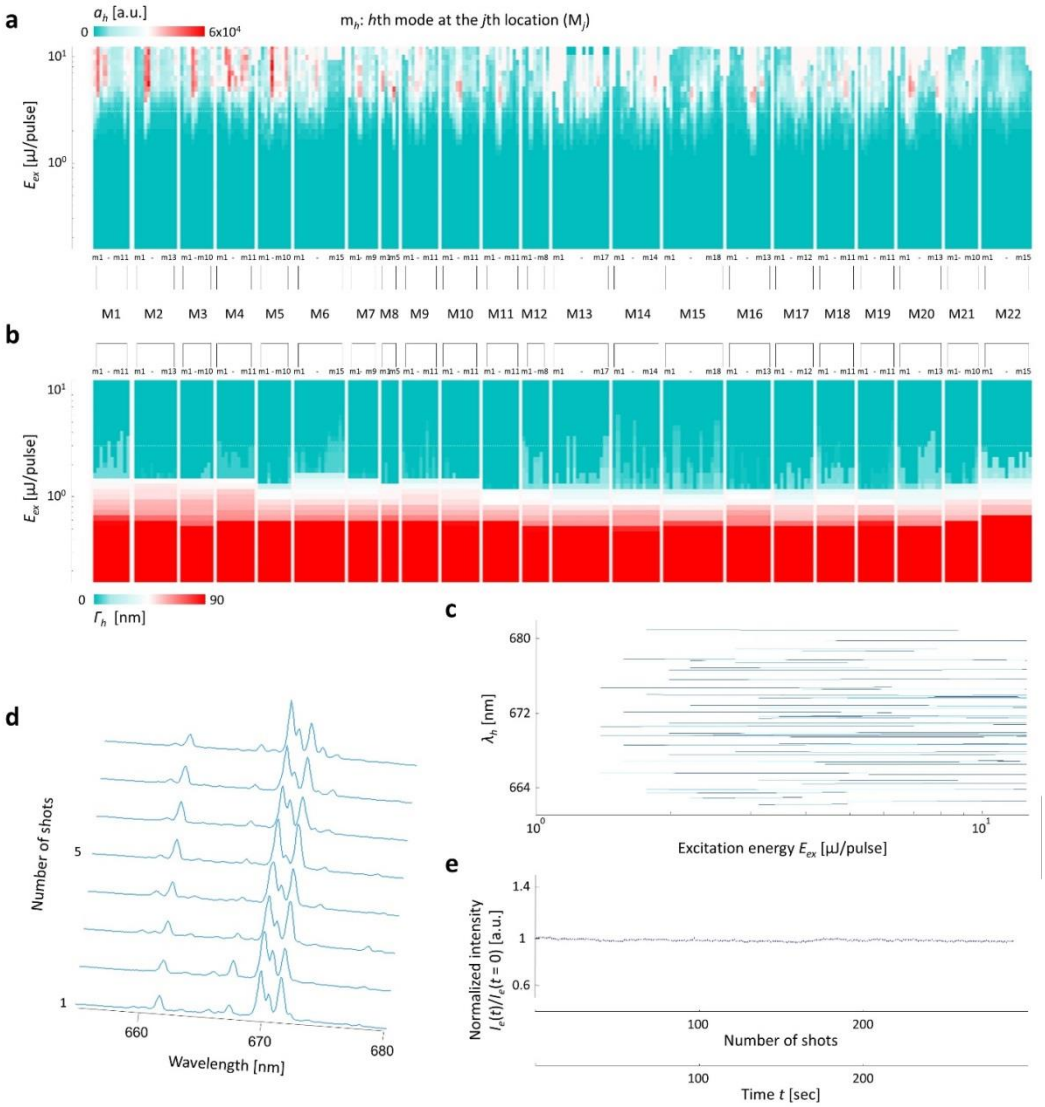

Extended Data Fig. 10. a_h, Γ_h, and λ_h from modal decompositions.
a–**c**, Intensity a_h (**a**), linewidth Γ_h in λ (**b**), and central wavelength λ_h (**c**) of lasing modes decomposed from $I_e(E_{ex}, \lambda)$. A total of 259 modes acquired at 22 different locations with a translation step of > 100 μm on the silk cocoon shell are analyzed. Each column of **a** and **b** indicates the evolution of a_h and Γ_h for the m_h single lasing mode as a function of E_{ex}. The Q factors (= ω_h/Γ_h) are evaluated at the threshold of each decomposed mode (blue solid lines). The white dashed lines mark the average lasing thresholds of the silk specimen (Fig. 6c). The data in **a**–**c** are used for the analyses in Fig. 6a–e. **d**, Spectra from single-shot excitation pulses at E_{ex} = 3.5 μJ/pulse in a fixed location. The series of single-shot spectra are almost identical. **e**, Shot-to-shot fluctuations of emission intensity. The emission intensity, normalized by the initial emission intensity $I_e(t)/I_e(t = 0)$, is stable over 300 seconds (or 300 successive excitation pulses).

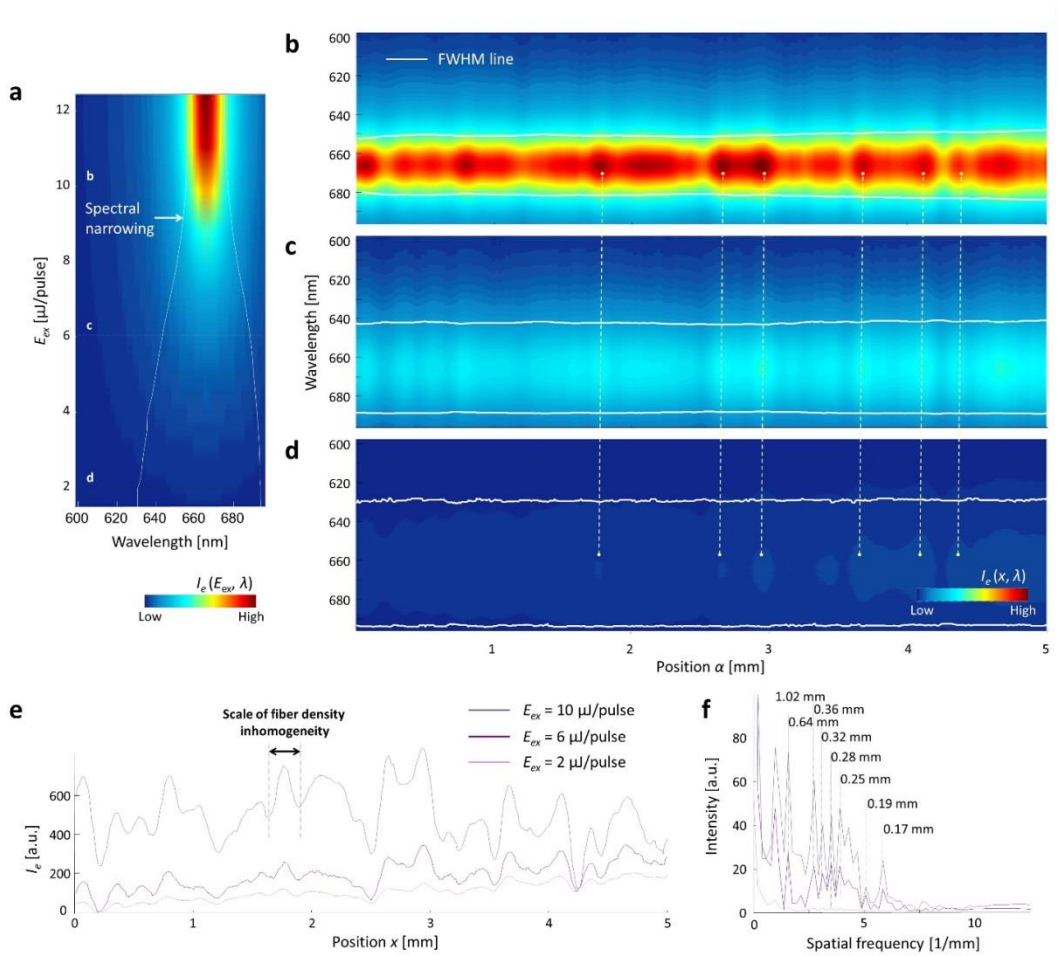

Extended Data Fig. 11. Disappearance of localized modes when fibers lose nanofibrils. **a**, $I_e(E_{ex}, \lambda)$ from the DCM-infiltrated paper specimen. The white solid lines mark the FWHMs of spectra that capture spectral narrowing of diffusive lasing (or amplified spontaneous emission). **b–d,** $I_e(\boldsymbol{r}, \lambda)$ at three different levels of excitation energy E_{ex} = 10, 6, and 2 μJ/pulse, marked in **a**. The FWHMs (white solid lines) are similar in spatial positions, while the emission intensity fluctuates. **e,** Spatial emission patterns in **b–d** at λ = 665 nm. The positions of peaks and lobes are nearly consistent over E_{ex} and the overall emission intensity increases simultaneously, because the emission fluctuation is originated from the local sample inhomogeneity. Analyzing distances between the lobes, the average length scale of fiber density inhomogeneity in the paper is ~ 215 μm. **f**, Spatial Fourier transforms of **e**. The spatial frequencies capture various length scales of fluctuations ranging from 170 μm to 1 mm.

1.6 Supplementary Methods

1.6.1 Imaging ultrastructure of silk

1.6.1.1 Scanning electron microscopy (SEM)

Using SEM, we imaged the surface of fractured fibroin filaments to investigate the morphology of nanofibrils, interfibrillar voids, silk fibers, and cocoons. The polymeric nature of silk proteins (i.e. fibroin), such as low atomic weight, low density protein, and rapid degradation to electron beam, often limits the use of electron microscopy[43,44]. Thus, the specimens were coated with platinum (Pt) for 60 seconds using a Cressington sputter coater (Ted Pella, Inc). The specimens were imaged using a NOVA nanoSEM field emission scanning electron microscope (FEI, Co) with an Everhart-Thornley detector or a high-resolution through-the-lens detector (TLD) at an accelerating voltage of 5kV. The SEM micrographs clearly show numerous individual nanofibrils separated by voids (Fig. 1b, c).

1.6.1.2 Transmission electron microscopy (TEM)

Using TEM, we imaged the cross-section of nanofibrillar structures in silk fibers to characterize their sizes and interfibrillar spaces. Typically, TEM is more challenging for imaging the ultrastructure of silk fibers[43-45]: 1) Silk fibroin filaments are composed of low atomic weight and low density protein elements (well-established metal staining methods are not currently available). 2) Silk proteins are subject to rapid degradation upon electron beam irradiation. 3) Ultrathin sections with proper orientations (i.e.

transverse and longitudinal cross sections) of nanofibrils are difficult. Thus, we made use of a two-step metal staining method for enhancing the image contrast of nanofibrils. The silk fiber specimens were fixed overnight with osmium tetroxide (OsO_4) vapor and then were infiltrated with Spurr's resin. After polymerization, the specimens were sectioned with a thickness of 100 nm. The sections underwent post staining with uranyl acetate in 70% methanol in five minutes and lead citrate in three minutes. The specimens were examined using a Tecnai T20 transmission electron microscope at 200 kV with a lanthanum hexaboride filament (FEI, Co). Micrographs were captured using a Gatan camera (Gatan, Inc). The TEM micrographs show areas of nanofibrils, sericin, and interfibrillar voids (Fig. 1d−f and Extended Data Fig. 1a−c). Nanofibrils were delineated from the density contrast resulting from more electrically dense nanofibrils and less dense voids, due to metal staining. The distributions of nanofibril sizes and interfibrillar spaces were extracted by the binary images that were post-processed from the TEM micrographs (Extended Data Fig. 1a).

1.6.1.3 Molecular imaging of nanofibrils

As a S158A variant of mKate, mKate2 (far-red fluorescent proteins) is more pH-stable and has higher brightness at physiological pH[46] (Extended Data Fig. 2e). To express mKate2 in nanofibrils of silk filaments, we genetically engineered domesticated silkworms (*Bombyx mori* bivoltine strain and Extended Data Fig. 2a), by means of silkworm transgenesis using germline transformation[47-49]. The transformation vector

p3xP3-EGFP-pFibH-mKate2 was constructed as the *piggyBac*-derived vector and was injected with a helper vector pHA3PIG into pre-blastoderm embryos[50] (Extended Data Fig. 2b). The mKate2 gene was fused with N-terminal and C-terminal domains of the fibroin heavy chain promoter (pFibH), confirmed by high-performance liquid chromatography with tandem mass spectrometry (LC-MS/MS) (Extended Data Fig. 2c, d). The 3xP3-EGFP system allowed us for screening a large number of G1 broods to identify transgenic silkworms[51]. The hatched larvae and silkworms were reared at 25°C and were fed on mulberry leaves as well as an artificial diet. As a result, red fluorescence signals appear in the silk gland (Extended Data Fig. 2f), the silk cocoons (Extended Data Fig. 2g), and the nanofibrils (Extended Data Fig. 3).

1.6.2 Calculation of the localization length of light ξ

The localization length of light ξ is an intrinsic ensemble-averaged decay length of localized modes as a statistical property in a finite system. Thus, it is important to investigate numerous structures of statistical equivalence. Ensemble average transmittance $< T >$ over 100 realizations of nanofibrillar structures were computed at different system lengths L (Extended Data Fig. 4a, b)[52-54]. The logarithmic decay is stabilized beyond $L > 5$ μm and converges to a single exponential:

$$< \ln T > \approx -L / 2\xi \text{ ,} \qquad \text{(S1)}$$

which returns ξ = 4.5 µm. The field shape (i.e. spatial extension) is an alternative route to estimate ξ (Extended Data Fig. 4c, d)[16,30,54]. The spread of wavefunction is quantified by an inverse participation ratio (IPR):

$$\mathrm{IPR}\ \left(E\left(x\right)\right) = \frac{\int dx \left|E\left(x\right)\right|^4}{\left|\int dx \left|E\left(x\right)\right|^2\right|^2}. \qquad \text{(S2)}$$

This length parameter relates ξ such that 1/IPR($E(x)$) = 2ξ, which enables to model an exponential field peak of a localized mode:

$$E\left(x\right) \sim \frac{e^{-|x|/2\xi}}{\sqrt{2\xi}}. \qquad \text{(S3)}$$

In Fig. 2a, the field patterns are in good agreement with the expression of Eq. S3, when ξ is substituted with their spreads of 1/IPR.

1.6.3 Measurements of the mean free path length of light

When transmission is supported by N transverse modes, $\xi \sim Nl$ [55,56], where l is the mean free path length of light. For anisotropic scattering, this characteristic length may also be defined using the scattering mean free path length l_s or the transport mean free path length l_t [18,28,57,58]. For biological and natural tissue, l can be considered as l_s such that

$$l_s = \frac{1}{\mu_s} = (1 - \left\langle \cos\ \theta \right\rangle) l_t, \qquad \text{(S4)}$$

where <cos ϑ> is the scattering anisotropy factor, μ_s is the scattering coefficient, and l_t is the transport mean free path length, which is measurable by coherent backscattering of light[3-5,59,60]. For a white silk cocoon specimen, the angular profile of coherent

backscattering returns l_t = 16 μm (Extended Data Fig. 5b). Indeed, light scattering in biological and natural tissue is often highly anisotropic ($l_s \neq l_t$)[2,61,62], while typical optical materials are isotropic ($l_s = l_t$). This difference originates from the scattering phase function $p(\bar{s}, \bar{s'})$, which is a probability of scattering into the direction $\bar{s'}$ from $\bar{s}$, leading to interpret light propagation from a particle standpoint[2]:

$$\frac{\partial R(\bar{r}, \bar{s})}{\partial s} = -(\mu_a + \mu_s) R(\bar{r}, \bar{s}) + \frac{\mu_s}{4\pi} \int_{4\pi} R(\bar{r}, \bar{s'})\, p(\bar{s}, \bar{s'})\ d\Omega', \quad \text{(S5)}$$

where $R(\bar{r}, \bar{s})$ is the radiance at position $\bar{r}$ traveling in the direction $\bar{s}$, $d\Omega'$ is the unit solid angle about $\bar{s'}$, and μ_a is the absorption coefficient. For $p(\bar{s}, \bar{s'})$, the overall directionality of scattering can be quantified, assuming symmetric scattering around the incidence direction $p(\bar{s}, \bar{s'}) = p(\theta)$:

$$\left\langle \cos\theta \right\rangle = \int_0^{\pi} p(\theta) \cos\theta\, 2\pi \sin\theta\ d\theta, \quad \text{(S6)}$$

where ϑ is the angle between $\bar{s'}$ and $\bar{s}$. To measure <cos ϑ> experimentally, an integrating sphere measurement with an inverse adding-doubling computation was conducted[63] (Extended Data Fig. 5c). For the white silk cocoon, it is likely that the light tends to scatter in the forward direction with <cos ϑ> = 0.78, returning l_s = (1− <cosϑ>) × 16 μm = 3.5 μm.

1.6.4 Discussion on the validity of optical transmission matrix measurements

For <cos ϑ> = 0.78 of the silk specimen, the angular dependence of scattering $p(\vartheta)$ is estimated using the Henyey-Greenstein phase function[2,64]:

$$p(\theta) = \frac{1}{4\pi} \frac{1 - \langle \cos\ \theta \rangle^2}{(1 + \langle \cos\ \theta \rangle^2 - 2\langle \cos\ \theta \rangle \cos\ \theta)^{3/2}} . \quad \text{(S7)}$$

As shown in Extended Data Fig. 5c, the probability of backward and side scattering is negligible compared to forward scattering with an effective scattering angle of $\cos^{-1}(0.78) \approx 39º$. This indicates that the angular passband of $\sin^{-1}(\text{NA}) = 64º$, where NA = 0.9 of the objective lenses (Fig. 4a), mostly covers the wave through the outgoing channels *b* of the silk specimen as well as effectively couples the input illumination into the incident channels *a*. Thus, it is unlikely that the optical transmission matrix measurements underestimate the value of dimensionless conductance *g* of the silk specimen, in spite of the finite solid angle of the objective lenses.

CHAPTER 2. HYBRIDIZED/COUPLED RESONANCES IN NACRE

2.1 Introduction

Interactions of electromagnetic waves with irregular and open structures are commonly considered to be inefficient, although disordered systems can be effectively used to identify disorder-induced resonances for enhanced confinement and transport.[7,37,65,66] Light amplification in such media[8,67-70] requires high excitation power and has low energy conversion efficiency, hampering its practical and widespread applications. Electrical excitation schemes have also been used to avoid high-power short pulse optical excitation.[71-73] To overcome the intrinsic limitations of disordered systems, simultaneous utilization of multiple resonances can be an effective approach for efficiently exciting disordered resonators. Indeed, multiple resonances can be coupled to form modes overlapped both in space and frequency (also known as necklace states): A collection of these modes can be hybridized into a long chain with multiple peaks in intensity. Hybridized/coupled states have often been studied in two regimes defined by the degree of spectral mode overlap (i.e. Thouless number or fundamental localization parameter): mode spacing $\Delta\omega <$ linewidths $\delta\omega$ and $\Delta\omega \geq \delta\omega$.[74-80]

Natural nacre can serve as intriguing low-dimensional photonic nanostructures to capitalize on hybridized multiple resonances for enhanced light-matter interactions. From a mechanical standpoint, as nanocomposites found in the inside layers of abalone shells, nacre has received considerable attention:[81-86] The mechanical and structural properties of nacre of abalone shells have been intensively studied to better understand how they deform and fracture in terms of plasticity and toughness. Indeed, nacre has provided valuable clues for synthesizing materials that mimic their excellent mechanical and structural properties.[87-89] From an optical standpoint, nacre has been studied to better understand the unique colors in terms of diffraction from fine-scale grating structures on the shell surface and interference from the inner nacreous layers.[90-92] In particular, photonic band states, which imply perfect ordered nanostructures, are speculated to play an important role in the distinct colors of abalone shells and pearls.[93,94] However, these unique nanostructures of nacre have not yet been exploited as optical resonators.

We report that hybridized/coupled multiple resonances can be possible underlying states for boosting light amplification and lasing in nacre, because nacre is a partially disordered nanostructure with an extremely large number of parallel layers. Although other previously identified natural/biological materials are often inappropriate for direct use in photonics,[95] nacre serves as an immediately exploitable nanocomposite to study multiple resonances in low dimension. In particular, the internal field intensity of coupled states in layered structures was investigated using large scale microwave

experiments while nonlinear effects could not be studied.[77,78] In photonics, mechanisms of necklace/coupled states, by which light can be effectively coupled into lasing states, have not yet been studied, in part because photonic structures realizing and visualizing hybridized/coupled states are rare in nature and challenging to synthesize. In this study, we investigate hybridized multiple resonances and visualize their local energy density distributions, in which gain media make such resonances readily detectable. First, we quantify the physical and nanostructural properties of nacre of green abalone shells. Second, using numerical simulations based on the transfer matrix method, we study the role of hybridized multiple resonances in light transport and amplification. Third, we conduct photoluminescence and lasing experiments using nacre.

2.2 Results

2.2.1 Nanostructures and photonic properties of nacre

We prepared nacre specimens from shells of *Haliotis fulgens* (green abalone and inset of Fig. 1a): Large strips from the shell were cut using a precision saw. The calcitic and growth layers were removed using a fine grinder. We also removed the organic materials (i.e. protein and chitin) that fill the gap of ceramic (i.e. aragonite) layers using sodium hypochlorite. In particular, the resulting gap allowed fluorescence dyes to easily smear inside nacre for fluorescence confocal microscopy (Fig. 1a).

Fig. 1a shows that nacre has inorganic ceramic (i.e. aragonite) tablets of 473 ± 50 (standard deviation, SD) nm arranged in layers. The ceramic tablets are separated by a gap of 40 ± 10 (SD) nm (Fig. 1b), which is occupied by organic materials (i.e. protein and chitin). Nacre contains an extremely large number of parallel layers. Nacre specimens with a thickness of 2 mm can contain up to ~ 4,000 alternating aragonite and gap layers. Aragonite has metastable pseudo-hexagonal crystal structures (Fig. 1c), resulting in an optically dense form of calcium carbonate ($CaCO_3$) polymorphs. Thus, nacre can be an ideal nanocomposite with alternating layers with low and high refractive indices (refractive index of aragonite n_a ~ 1.65 – 1.68 and Fig. 2b). Moreover, the ceramic layers have a thickness comparable to the wavelength of the visible light. In this case, the phase can be randomized quickly as the wave propagates, leading to a short localization length.

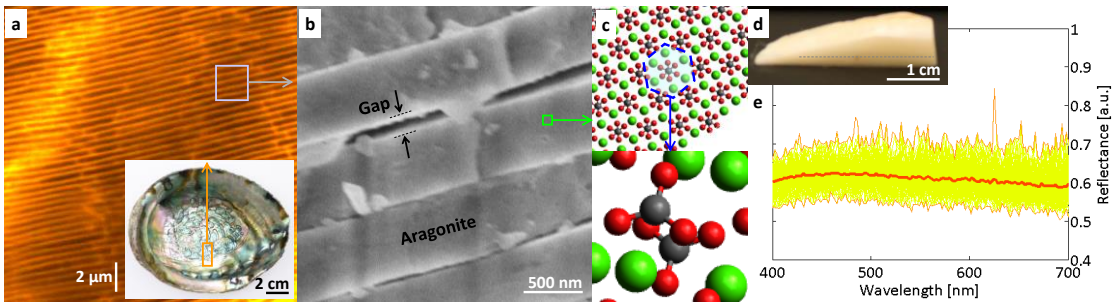

Fig. 1. Nanostructures and photonic properties of *Haliotis fulgens* (green abalone). **a,** Confocal fluorescence microscopy image of nacre infiltrated with rhodamine 6G (Rh6G) after deproteinization. Inset: Photograph of the original abalone shell. **b**, Scanning electron microscopy (SEM) image of a brick-mortar nanostructure in nacre. **c**, The molecular architecture of aragonite viewed from the C axis (top) and off the C axis (bottom). **d**, Photograph of deproteinized nacre. **e**, Reflectance spectra (spectral resolution = 2 nm) from deproteinized nacre, averaged from ~ 100 spectra.

Fig. 1d shows that nacre has a diffuse white color after deproteinization, although the bulk aragonite crystal is known to be optically translucent or transparent. The original captivating color of abalone nacre (inset of Fig. 1a) should be ascribed to both pigmentation of the organic materials and optical effects of the aragonite layers. The averaged reflectance spectrum from deproteinized thick nacre (Fig. 1e) is relatively flat in the visible wavelength range of λ = 400 – 700 nm (assuming the corresponding perfect periodic structure, the bandstop is λ ~ 555 – 569 nm): Reflectance spectra were obtained within a small angular cone of ± 2° in the backward direction[96] while deproteinized nacre was placed in a methanol solution (i.e. dye solvent). Indeed, the ratio of a SD to an averaged thickness of the aragonite- and gap-combined layer, which can be quantified as morphological disorder, is $\sqrt{50^2 + 10^2}/(473 + 40) \approx 0.1$. Thus, the unique color of nacre is significantly attributed to the disordered multilayered nanostructures.

2.2.2 Theoretical consideration of hybridized states in nacre

Given the highly multilayered nanostructures of nacre, we numerically investigated behavior of hybridized states assuming one-dimensional (1D) disordered cavities. For quasimodes and lasing modes in nacre's nanostructures, we used the transfer matrix method[96,97] with complex and frequency-dependent refractive indices implementing linear gain,[98,99] as shown in Fig. 2. By incorporating a spatially modulated frequency-dependent susceptibility $\chi_g(z, k = 2\pi/\lambda)$ in the refractive index of gap n_g, the

homogeneous field amplification and the linear gain of dye molecules can be simulated such that

$$n_g(z,k) = n_r(z,k) + in_i(z,k) = \sqrt{n_{g(nr)}^2(z,k) + \chi_g(z,k)}$$

$$\text{and } \chi_g(z,k) = \frac{A_m N_{ex}(z)}{k_a^2 - k^2 - ik\Delta k_a},$$

where n_r and n_i (< 0) are the real and imaginary parts of the refractive index, $n_{g(nr)}$ is the refractive index of the nonresonant background material, z is the spatial coordinate, A_m is a material-dependent constant, N_{ex} is the density of excited atoms, k_a is the atomic transition frequency (i.e. peak frequency of dye molecules), and Δk_a is the spectral linewidth of the atomic resonance (i.e. spectral width of spontaneous emission of dye molecules). Both Re $\chi_g(k)$ and Im $\chi_g(k)$ are proportional to the density of excited atoms N_{ex} determined by the excitation energy. It should be noted that this linear gain model is only valid at or below the threshold.

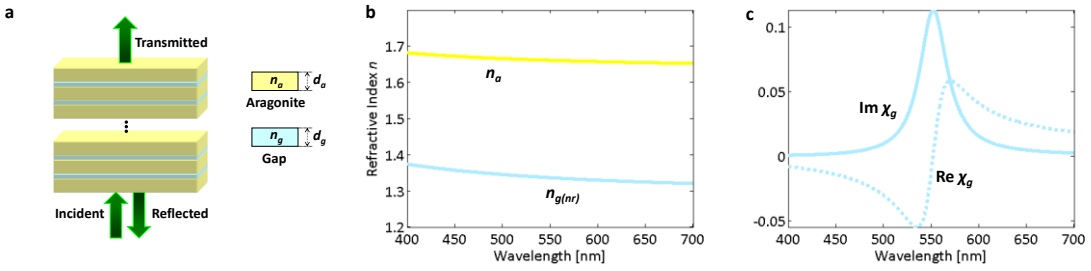

Fig. 2. Calculation of hybridized/coupled states and light amplification.
a, Schematic diagram of the experimental configuration. **b**, Dispersion curves of aragonite and gap layers. **c**, Real and imaginary parts of susceptibility of gain χ_g (λ).

We accounted for the nacre's nanostructures using the structural parameters obtained from confocal microscopy and scanning electron microscopy (Fig. 1a, b). A similar level of morphological disorder was set by randomly varying the aragonite thickness and the gap distance in the ranges of d_a = 473 ± 50 (SD) nm and d_g = 40 ± 10 (SD) nm, respectively. The 1D nanostructures consisted of a total of 2,000 layers alternating aragonite and gap, corresponding to a system length of L_T ~ 0.5 mm. The wavelength-dependent refractive indices of aragonite and gap (methanol) were obtained from the experimental data[100,101] and their dispersion curves are shown in Fig. 2b. As low dye concentrations were used in later lasing experiments, the real part of the refractive index of dye solutions n_g can be assumed to be close to that of the solvent itself (i.e. methanol).[102] Fig. 2c shows the real and imaginary parts of χ_g over the wavelength for the gain medium in the gap. For the solution of rhodamine 6G (Rh6G), k_a = 11.38 μm^{-1} (551 nm) and Δk_a = 0.72 μm^{-1} (35 nm) were obtained from the experimental fluorescence spectra. Using the optical and geometrical parameters closely mimicking the experimental conditions, a 1D localization length ξ (= $-2L_T / <\ln T>$, where < … > stands for averaging over multiple realizations) was estimated that ξ = 37.2 μm. Thus, the system is in a localized regime $L_T >> \xi$.

Fig. 3a shows calculated transmittance spectra T and internal field intensity I of resonance modes when gain is absent (quasimodes). As indicated by the representative cases (dotted boxes in Fig. 3a), we categorized the coupling status into isolated modes and hybridized states. Hybridized states are further divided into two groups: i) mode

spacing $\Delta\omega$ < linewidths $\delta\omega$ and ii) $\Delta\omega \geq \delta\omega$. While both groups can be considered as coupled resonances with a different level of coupling, each can be identified using the

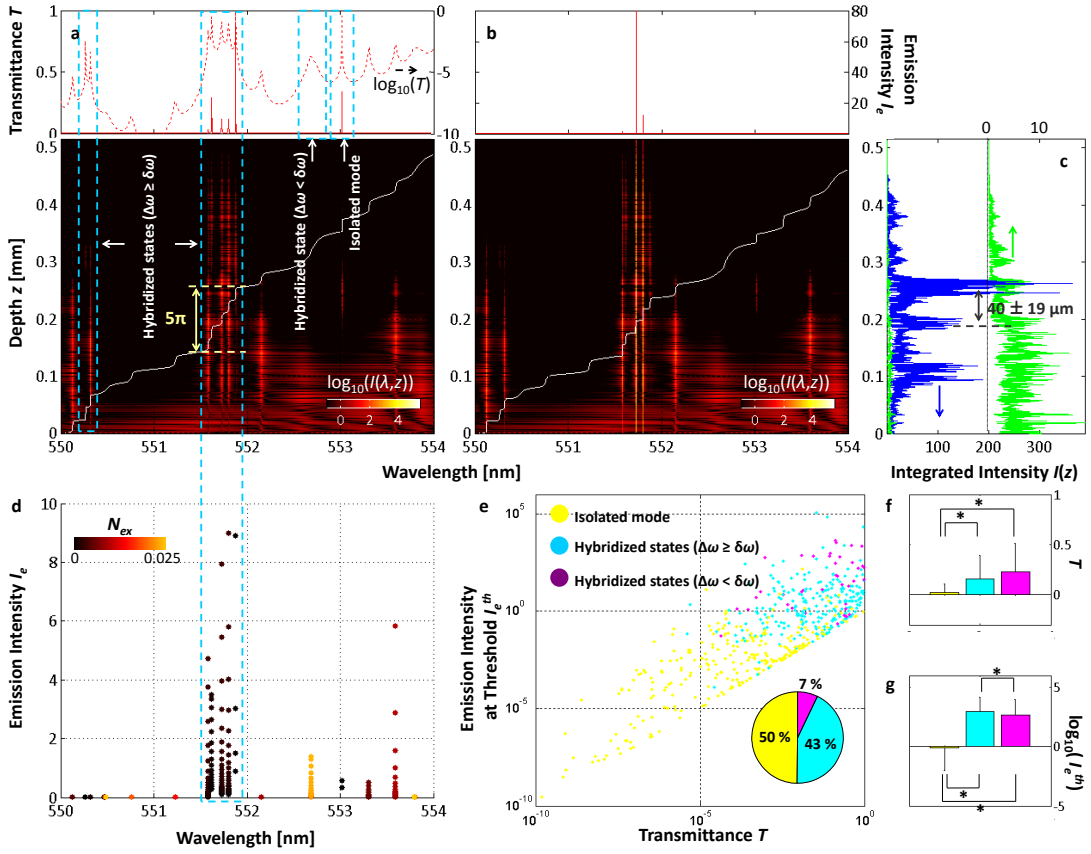

Fig. 3. Hybridized states and isolated modes in nacre and their amplification. **a,** Transmittance spectra T and $\log_{10}(T)$ (solid and dashed line in upper panel, respectively). Internal field intensity I (lower panel) of quasimodes (without gain). The white solid line is a phase change in the transmittance spectra. **b,** Emission spectra I_e (upper panel) and internal field intensity I (lower panel) of lasing modes (with gain). **c,** Spatial profiles of integrated quasimodes (green curve) and lasing modes (blue curve) horizontally shifted for visual clarity. **d,** I_e of lasing modes as a function of the density of excited atoms N_{ex}. **e** Emission intensity at the threshold of I_e^{th} (lasing mode) versus T (quasimode) from 32 different disorder configurations. Inset: Occurrence probabilities of two different hybridized states and isolated modes. **f, g** Characteristics of I_e^{th} and T of different states and modes. The colors of the data-points in **e** match with the states in the horizontal axes of f&g. * denotes statistically significant differences. The error bars are SDs.

accumulated phase shift[99] and the valleys between peaks in $\log_{10}(T)$[80] in addition to the fundamental localization parameters.

In particular, the transmission spectrum in the range of λ = 551.5 – 552 nm includes five narrow peaks close to one another. This group ($\Delta\omega \geq \delta\omega$) is the collection of localized modes (lower panel in Fig. 3a) which are overlapped in frequency and have similar field distributions in space.[77,78] In this case, the relatively high valleys between the narrow adjacent peaks become obvious in $\log_{10}(T)$. Interestingly, when $\Delta\omega \geq \delta\omega$, the spatial field distributions are extended over the whole structure, consisting of multiple localized resonances in space, while individual $\delta\omega$ is still narrow. These states would have lifetimes shorter yet comparable to the single localized modes, because $\delta\omega$ of the adjacent peaks stays narrow while still having the very low valleys in the linear scale of T. However, when $\Delta\omega < \delta\omega$, the hybridized states would have much shorter lifetime because weak mode splitting occurs, resulting in a single broadened peak. Thus, in the nominally localized systems, the hybridized states with $\Delta\omega \geq \delta\omega$ are distinguishable from the hybridized states with $\Delta\omega < \delta\omega$. In this respect, the hybridized states with $\Delta\omega \geq \delta\omega$ are hereafter referred to as hybridized localized states.

Upon the introduction of the density of excited atoms $N_{ex} = 3 \times 10^{-3}$ which is spatially uniform in each gain region, the emission intensity I_e of the hybridized localized state (within 551.5 – 552 nm) is higher than those of the other hybridized states and isolated modes (Fig. 3b). As the gain increases, I_e of the hybridized localized state is

amplified together (Fig. 3d). To also compare with spatial images of intensity obtained using a microscopy imaging setup with finite bandwidth (Fig. 4a), the internal intensity is integrated such that $I(z) = \int I(\lambda, z)\mathrm{d}\lambda$ over the range λ = 550 – 554 nm. When the internal field is averaged over the wavelength range, the passive hybridized localized state (without gain) is hidden (green curve in Fig. 3c). However, in the presence of gain (blue curve in Fig. 3c), the multiple peaks of the hybridized localized state dominantly emerge with an inter-resonance spacing of 41 ± 19 μm on the order of ξ, indicating a high coupling efficiency. In other words, gain allows the clear identification of the hybridized localized states formed from regularly spaced resonances in space.

To understand the light transport and amplification properties of the hybridized states, we analyzed 546 spectral peaks from 32 different configurations of 1D disordered cavities (Fig. 3e). The occurrence probability of all hybridized states (the number of the peaks in the hybridized states over the number of the total peaks) is similar to that of the isolated modes (inset of Fig. 3e). The overall tendency (Fig. 3e, f) is that the transmittance T of the hybridized states (both $\Delta\omega < \delta\omega$ and $\Delta\omega \geq \delta\omega$) is ~ 7.9 times higher than that of the isolated modes, revealing that their main characteristic is enhanced transport or tunneling. In the hybridized localized states, the individual modes are overlapped in frequency with similar shapes spanning over the whole structure, thus being collectively excited. In addition, their spatially extended fields can utilize larger areas with gain. As a consequence of synergical amplification, I_e of the

hybridized localized states ($\Delta\omega \geq \delta\omega$) is 1.1×10^3 times higher than that of the isolated modes (Fig. 3g). I_e of the hybridized localized states is twice higher than that of the hybridized states with $\Delta\omega < \delta\omega$. Interestingly, when $\Delta\omega < \delta\omega$, the hybridized states are still significantly amplified compared with the isolated modes (Fig. 3g), although their passive states appear to have the degenerate localized properties with the broadened $\delta\omega$.

The enhanced transport effect of the hybridized localized states can provide additional benefit for achieving efficient light amplification, because the fields at both excitation and emission bands can overlap spatially deep into the structure.[103] It should be noted that as implied in Fig. 1e given the disordered nanostructures, the hybridized states can occur at any wavelength ranges. In contrast to the previous study on isolated localized modes,[103] our results show that in the structures with an extremely large number of layers (> 2,000), resonant tunneling through the isolated localized modes is not as efficient as the hybridized states for light amplification and lasing.

2.2.3 Photoluminescence experiments using nacre

We conducted lasing experiments in a similar manner as in our previous studies:[39,104] As shown in Fig. 4a, a frequency-doubled Q-switched Nd:YAG laser (pulse duration of 400 ps and and λ of 532 nm) was used to optically excite each specimen (S in Fig. 4a). The excitation beam (diameter = 1 mm) from the pulsed laser was illuminated on the specimen via a low numerical aperture objective (5×). The spot size at the focal plane

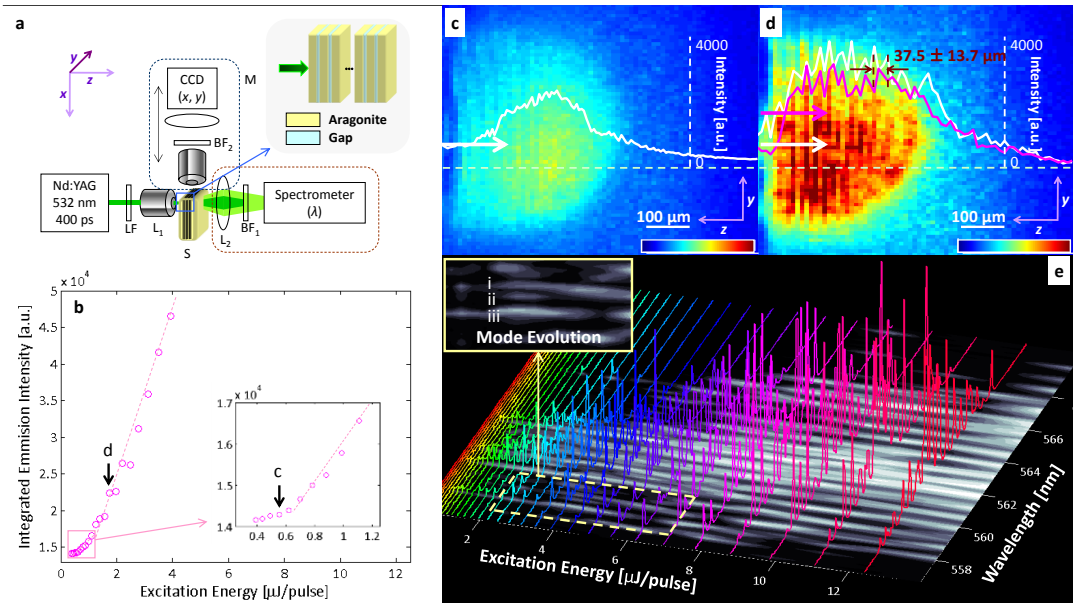

Fig. 4. Photoluminescence experiments using abalone nacre.
a, Schematic diagram of the experimental setup. **b**, Integrated emission intensity from Rh6G-infilterated nacre (pink data-points) and white paper (black data-points) as the excitation energy increases. The intensity is integrated within the same wavelength range for both specimens. **c, d**, Pseudocolor microscopic images of spatial fields averaged over wavelength through the 10-nm (FWHM) bandwidth filter: **c**, Below the threshold (= 0.56 μJ/pulse) and **d,** above the threshold (= 1.98 μJ/pulse). The solid curves are longitudinal intensity distributions at different horizontal cross-sections. **e,** Emission spectra as the excitation energy increases. The spectra are also projected onto the grayscale map.

was 20 μm in diameter and strong focusing onto the specimen surface was avoided. To vary the excitation energy, a linear variable neutral density filter (LF in Fig. 4a) was used in the delivery arm. The emitted light on the other side were collected by a fiber bundle through a lens (L_1 & L_2 in Fig. 4a) and a bandpass filter (BF_1 in Fig. 4a) (λ = 600 ± 70 nm) and coupled to a spectrometer (spectral resolution = 0.2 nm). The data acquisition time was 0.2 second, in which 100 excitation pulses were accumulated. In addition, we placed the customized microscopy imaging setup (M in Fig. 4a) to image the spatial

distribution of emission intensity inside the structures via a bandpass filter of λ = 568 ± 10 (FWHM) nm (BF_2 in Fig. 4a), when the excitation illumination was near the edge. Deproteinized nacre specimens with a thickness of ~ 2 mm were doped with different laser dyes. Four dyes were used at low concentrations of ~ 0.5 mg/ml: Rh6G, rhodamine B (RhB), and rhodamine 101 (Rh101) all in methanol, as well as DCM in dimethyl sulfoxide.

We first observed the signature of hybridized localized states by imaging the spatial distributions of the emission intensity inside Rh6G-infilterated nacre, when the excitation illumination was perpendicular to the layers near the edge of nacre. Below the threshold (= 0.62 μJ/pulse and Fig. 4b), the emission intensity from Rh6G-infiltrated nacre is concentrated within ~ 0.5 mm and the spatial distribution is relatively smooth (Fig. 4c), because several randomly distributed modes are averaged spatially within the spectral width of the bandpass filter of λ = 568 ± 10 (FWHM) nm (BF_2 in Fig. 4a). However, at an excitation energy of ~7 μJ/pulse (pink circles in Fig. 4b), the clear signature of hybridized localized states is observed (Fig. 4d): The intensity exhibits several peaks inside nacre and stretches through the specimen. Several peaks appear along the longitudinal direction with a separation of ~ 37.5 ± 13.7 (SD) μm. This fairly consistent separation of intensity peaks indicates that the hybridized states are selectively distinguished via lasing action. Indeed, this inter-resonance spatial separation obtained from the experimental visualization of the local energy disposition in nacre is in agreement with the numerical result (Fig. 3c).

As the excitation energy increases, spectral evolution is clearly seen in the grayscale intensity map of Fig. 4e and the inset. Multiple narrow emission peaks rapidly emerge from Rh6G-infiltrated nacre as the excitation energy increases. Immediately above the threshold, new lasing peaks appear (e.g. mode i, ii, and iii) and then some initial peaks disappear (e.g. mode iii). At higher excitation energy (> 9 μJ/pulse), the spectral positions of the multiple peaks become stabilized. Indeed, such dynamical spectral evolution of mode competition/suppression as a function of the excitation energy has been studied mainly in theoretical studies,[30,105] due to the inefficient nature of high-dimensional disordered resonators.

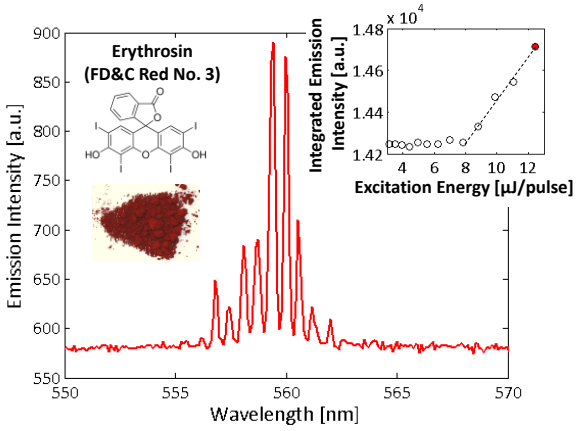

Fig. 5. Food dye lasing.
Representative multimode emission spectrum above the threshold (excitation energy = 12.4 μJ/pulse as indicated the red dot in the right inset). Left inset: Structural formula of erythrosine and photography of erythrosine powders. Right inset: Emission intensity integrated within λ = 547 – 572 nm as a function of the excitation energy.

To further support the efficient nacre resonator, we utilized erythrosine (FD&C Red No. 3) that is approved by the FDA for food coloring. We measured quantum yields (QYs) of fluorophores, including erythrosine, in a similar manner as in our previous

study.[106] The QY of erythrosine in methanol (= 2.5 %) is 37.5 times lower than those of typical laser dyes (e.g. Rh6G = 94.5 %). Surprisingly, nacre still allowed us to achieve multimode lasing action using erythrosine (Fig. 5 and the threshold ~ 8 μJ/pulse). This result supports the idea that nacre provides a means to amplify extremely weak fluorescence light to readily detectable sharp stimulated emission peaks.

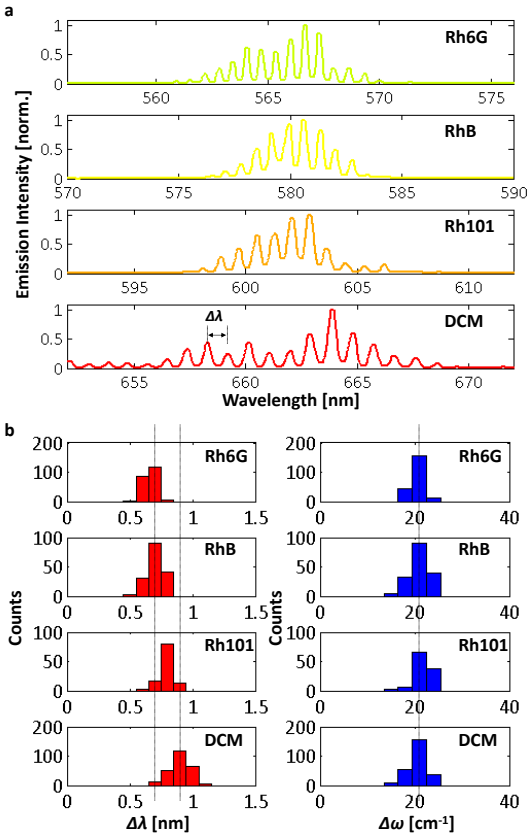

Fig. 6. Spectral characteristics of lasing emission.
a, Emission spectra at the excitation energy of 15 – 20 μJ/pulse above the lasing thresholds. **b**, Wavelength spacing $\Delta\lambda$ and frequency spacing $\Delta\omega$ between adjacent peaks, respectively.

Finally, we investigated gain competition and saturation, which can easily be manifested in efficient resonators. We applied excitation energy (15 – 20 μJ/pulse) higher than the lasing threshold and quantified the spectral spacing of discrete emission peaks. Representative multiple narrow emission peaks are shown in Fig. 6a. Interestingly, Fig. 6b reveals that the frequency spacing $\Delta\omega$ (in the unit of cm^{-1}) has a highly consistent value. This unique spectral characteristic of multimode lasing is attributable to high competition and saturation of gain.[30,105,107,108] As nacre has low dimensionality and inherently forms hybridized localized states, which are forced to share the same gain spatially, the local depletion of excited electrons from the lasing modes suppresses other spatially overlapped modes. The importance of hole burning in this characteristic is supported by the fact that $\Delta\omega$ from the nacre resonators is comparable to the homogenous linewidths of similar dye molecules measured at room temperature.[109] The highly stable and repeatable multimode lasing emission in nacre could potentially be considered as a precursor of spontaneous mode-locking, as demonstrated by exciting a large number of spatially overlapped resonances in disordered cavities.[110]

2.3 Conclusions

We report that hybridized/coupled multiple resonances in nacre allow collective excitation to synergistically enhance light amplification and lasing. Our study provides a foundation for natural/synthesized nacre materials that can be immediately exploited for developing economical photonic systems and for better understanding wave

interactions in complex media. In particular, nanoscale gaps in nacre could potentially be utilized to host/trap other nanomaterials for chemo/biosensor development. In addition, nacre can serve as a model system for addressing fundamental questions in low-dimensional systems.

2.4 Supplementary Methods

2.4.1 Lasing modes and quasimodes calculation in 1D

For lasing modes and quasimodes in nacre's nanostructures, we used the transfer matrix method (TMM)[97,111-113] with complex and frequency-dependent refractive indices implementing linear gain. The electromagnetic wave (*E* and *H*) of a given wavenumber *k* (= 2π/*λ*) propagating through *L* layers (Fig. 2a) at the normal incidence is described such that

$$\begin{bmatrix} E_1 \\ H_1 \end{bmatrix} = M \begin{bmatrix} E_{L+1} \\ H_{L+1} \end{bmatrix} = M_1 M_2 \cdots M_L \begin{bmatrix} E_{L+1} \\ H_{L+1} \end{bmatrix} \text{ and} \tag{S1}$$

$$M_l = \begin{bmatrix} \cos(kn_l d_l) & i\sin(kn_l d_l)/n_l \\ i\sin(kn_l d_l) n_l & \cos(kn_l d_l) \end{bmatrix},$$

where n_l and d_l are the refractive index and thickness of the l^{th} layer, respectively. By incorporating a spatially modulated frequency-dependent susceptibility $\chi_g(z, k)$ in the refractive index of gap n_g, the homogeneous field amplification and the linear gain of dye molecules can be simulated such that

$$n_g(z,k) = n_r(z,k) + in_i(z,k) = \sqrt{n_{g(nr)}^2(z,k) + \chi_g(z,k)} \text{ and} \tag{S2}$$

$$\chi_g(z,k) = \frac{A_m N_{ex}(z)}{k_a^2 - k^2 - ik\Delta k_a},$$

where n_r and n_i (< 0) are the real and imaginary parts of the refractive index, $n_{g(nr)}$ is the refractive index of the nonresonant background material, z is the spatial coordinate, A_m is a material-dependent constant, N_{ex} is the density of excited atoms, k_a is the atomic transition frequency (i.e. peak frequency of dye molecules), and Δk_a is the spectral linewidth of the atomic resonance (i.e. spectral width of spontaneous emission of dye molecules). This linear gain model is only valid at or below the threshold. After implementing $n(z, k)$ in the characteristic matrix M, the transmittance T and the reflectance R can be obtained as follow:

$$T = \frac{2n_0}{n_0 M_{11} + n_0 n_s M_{12} + M_{21} + n_s M_{22}} \text{ and} \qquad \text{(S3)}$$

$$R = \frac{n_0 M_{11} + n_0 n_s M_{12} - M_{21} - n_s M_{22}}{n_0 M_{11} + n_0 n_s M_{12} + M_{21} + n_s M_{22}},$$

where n_0 and n_s are the refractive indices of the bottom and top media (Fig. 2a). For spatial field distributions, the electric intensity I (= $E \cdot E^*$) can be computed.

We accounted for the nacre's nanostructures using the structural parameters obtained from confocal microscopy and scanning electron microscopy (Fig. 1a&b). A similar level of disorder was set by randomly varying the aragonite thickness and the gap distance in the ranges of d_a = 473 ± 50 (SD) nm and d_g = 40 ± 10 (SD) nm, respectively. The one-dimensional (1D) nanostructures consisted of a total of 2,000 layers alternating

aragonite and gap, corresponding to a system length of L_T ~ 0.5 mm. To quantify the disorder strength, we used a ratio of a SD to an averaged thickness of aragonite and gap layers: The ratio was ~ 0.1 (= $\sqrt{50^2 + 10^2}/(473 + 40)$). The wavelength-dependent refractive indices of aragonite and gap (methanol) were obtained from the experimental data[100,101] and their dispersion curves are shown in Fig. 2b. Fig. 2c shows the real and imaginary parts of χ_g over the wavelength for the gain medium in the gap. For the solution of Rh6G, k_a = 11.38 μm^{-1} (551 nm) and Δk_a = 0.72 μm^{-1} (35 nm) were obtained from the experimental fluorescence spectra. Using the optical and geometrical parameters closely mimicking the experimental conditions, a 1D localization length ξ (= $-2L_T/ < \ln T >$, where < … > stands for averaging over multiple realizations) was estimated that ξ = 37.2 μm for 100 μm < L_T < 360 μm.

2.4.2 Statistical analysis

Kruskal-Wallis tests were used as a non-parametric analysis because normality and equal variance for parametric analyses were not validated. A Bonferroni correction method was used to adjust *p*-values for multiple comparisons.

2.4.3 Specimen preparations

We prepared 12 nacre specimens from shells of *Haliotis fulgens* (green abalone) as follows: Large strips from the shell were cut using a precision saw. The calcitic and growth layers were removed using a fine grinder. We also removed the organic

materials (i.e. protein and chitin) that fill the gap of ceramic (i.e. aragonite) layers using sodium hypochlorite. The thickness of the specimens was 2 mm, which corresponds to ~ 4,000 layers (= 2 mm / 500 nm). For comparison with the nacre's nanostructures in low dimension, we also used white paper (thickness = 2 mm) as highly disordered structures in high dimension (3D), as shown in Supplementary Fig. 1a. For photoluminescence experiments, five different dyes were used at low concentrations of 0.5 mg/ml: rhodamine 6G (Rh6G), erythrosine (also known as FD&C Red No. 3), rhodamine B (RhB), rhodamine 101 (Rh101) all in methanol, as well as DCM in dimethyl sulfoxide (DMSO). For reflectance and coherent backscattering measurements, the specimens were placed in a methanol solution (solvent for Rh6G) to match with the real part of the refractive index of the Rh6G solution. At low dye concentrations, the real part of the refractive index of dye solutions is close to that of the solvent itself[102].

2.4.4 Mean free path length measurements

To measure the scattering properties of the specimens, we performed reflectance and coherent backscattering measurements. For reflectance measurements, we obtained spectra backscattered within a small angular cone of ± 2° in the exact backward direction as previously described[96,106]. To assess the mean free pathlengths of light l_s in the specimens, we conducted coherent backscattering measurements as previously described[60], using a He-Ne laser (Supplementary Fig. 2a). The specimen was illuminated with the beam with a diameter of 3 mm and was rotated to remove speckle. The angular profiles of the nacre and paper specimens corresponded to l_s = 16.9 μm and 7.3

μm at 542 nm, respectively (Supplementary Fig. 2b, c). For electron microscopy images, we used a Hitachi S-4800 field emission SEM.

2.4.5 Photoluminescence experiments

We conducted lasing experiments in a similar manner as in our previous studies[39,104]. As illustrated in Fig. 3a, a frequency-doubled Q-switched Nd:YAG laser (pulse duration of 400 ps, repetition rate of 500 Hz, and λ of 532 nm) was used to optically excite each specimen (S in Fig. 3a). The excitation beam (diameter = 1 mm) from the pulsed laser was illuminated on the specimen via a low numerical aperture objective (5×). The spot size at the focal plane was 20 μm in diameter and strong focusing onto the specimen surface was avoided. To vary the excitation energy, a linear variable neutral density filter (LF in Fig. 3a) was used in the delivery arm. The emitted light on the other side were collected by a fiber bundle through a lens (L_1 & L_2 in Fig. 3a) and a bandpass filter (BF_1 in Fig. 3a) (λ = 600 ± 70 nm) and coupled to a spectrometer (spectral resolution = 0.2 nm). The data acquisition time was 0.2 second, in which 100 excitation pulses were accumulated. In addition, we also placed the customized microscopy imaging setup (M in Fig. 3a) to image the spatial distribution of emission intensity inside the structures via a bandpass filter of λ = 568 ± 10 (FWHM) nm (BF_2 in Fig. 3a), when the excitation illumination was near the edge.

2.4.6 Comparison with white paper

For simple comparison, we used white paper as commonly accessible 3D disordered structures (Supplementary Fig. 1a, b). The threshold of Rh6G-infilerated nacre is ~ 13 times lower and the conversion efficiency is ~14 times higher than those of paper (Fig. 3b), although the mean free pathlength of light in the nacre specimen (= 16.9 μm at 542 nm) is twice as large as the value in the paper specimen (= 7.3 μm at 542 nm) (Supplementary Fig. 2). The lasing emission from the white paper merely shows a spectral narrowing (amplified spontaneous emission) (Supplementary Fig. 1c).

2.4.7 Quantum yield measurements

We measured quantum yields (QYs) of fluorophores, including erythrosine, in a similar manner as in our previous study[106]. The excitation beam at 532 nm was illuminated on a 10-mm quartz cuvette containing the dye solution. The transmitted and emitted light from the specimen was collected via an optical fiber contacted on the cuvette at the opposite side and was analyzed with a spectrometer. Then, we determined unknown fluorescence QYs by using the fluorescence intensity of a fluorophore with a known QY (Supplementary Fig. 3):

$$\Phi_s = \Phi_R \left(\frac{dI_s^{FL} / dA_s}{dI_R^{FL} / dA_R} \right) \left(\frac{n_s^2}{n_R^2} \right), \quad \text{(S4)}$$

where Φ is QY, I^{FL} is the area under the fluorescence spectrum, A is the absorbance at the excitation wavelength ($0 \le A \le 1$), and n is the refractive index of the specimen. The

subscripts *S* and *R* denote the specimen to be determined and the reference substance, respectively. We used Rh101 in methanol as the reference substance (Φ_R = 0.95) and all of the experiments were done at room temperature. The measured QYs are summarized in Supplementary Table 1.

2.4.8 Supplementary Figures, Table, and Legends

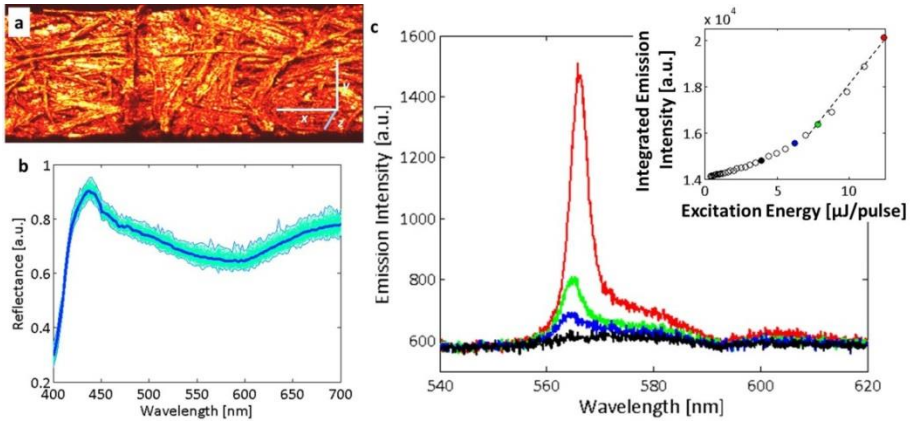

Supplementary Fig. 1. **Structural and physical properties of white paper.** **a** Pseudocolor reflectance confocal microscopy image of white paper. The scale bars: x = 200 μm, y = 200 μm, and z = 120 μm. **b** Representative reflectance spectra from white paper. ~100 spectra from different locations are plotted together. **c** Representative emission spectra from white paper infiltrated with Rh6G. **Inset:** Emission intensity integrated within λ = 557 – 581 nm and threshold of ~ 8 μJ/pulse. The paper lasing emission merely shows spectral narrowing (i.e. amplified spontaneous emission). The colors of the emission spectra match with those of the data-points in the inset.

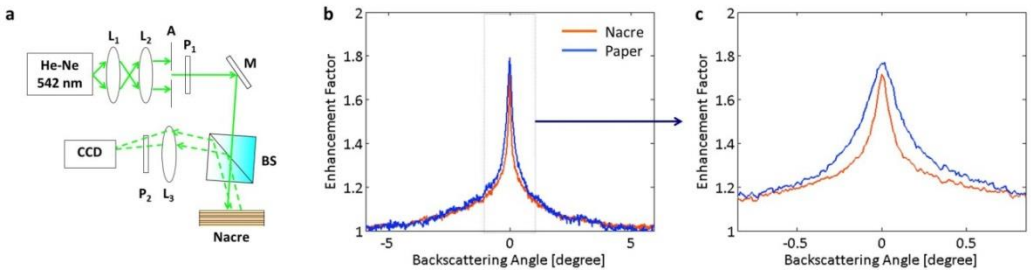

Supplementary Fig. 2. Coherent backscattering measurements for l_s. **a** Schematic diagram of the experimental setup: He-Ne, He-Ne laser (λ = 542 nm); $L_{1,2,3}$, lenses; A, apertures; $P_{1,2}$, polarizers; M, mirror; B, beam splitter; and CCD, camera. **b** and **c** Angular profiles of coherent backscattering from deproteinized nacre and white paper. For deproteinized nacre and white paper, l_s = 16.9 μm and 7.3 μm at 542 nm, respectively.

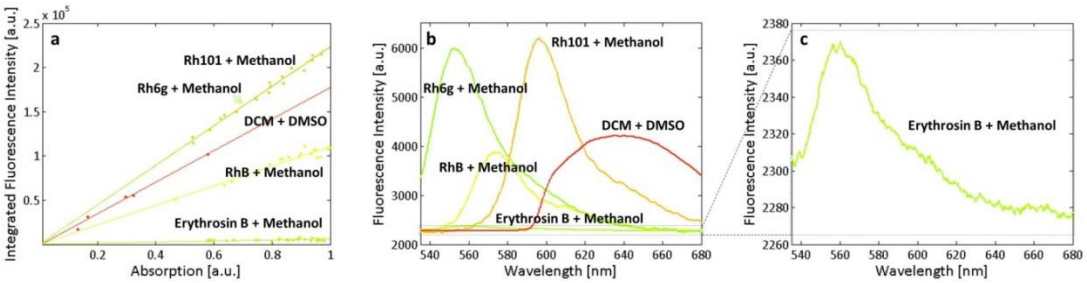

Supplementary Fig. 3. Quantum yield (QY) measurements of various dyes.
a Linear plots of integrated fluorescence intensity versus absorption. The slope of each dye solution is proportional to QY and the conversion into QY is achieved using the known reference (Rh101 in methanol). **b** and **c** Fluorescence emission spectra at an absorption of 0.8.

Supplementary Table 1. Quantum yield for different gain molecules

Dye solution	Quantum yield (QY)
Rh101 in methanol	95.0 % (Φ_R)
Rh6G in methanol	94.5 %
RhB in methanol	46.8 %
DCM in DMSO	75.0 %
Erythrosine in methanol	2.5 %

REFERENCES

REFERENCES

1 Boas, D. A., Pitris, C. & Ramanujam, N. *Handbook of Biomedical Optics*. (CRC Press, 2011).

2 Tuchin, V. V. *Tissue optics: Light scattering methods and instruments for medical diagnosis*. 3 edn, (SPIE-The International Society for Optical Engineering, 2015).

3 van Albada, M. P. & Lagendijk, A. Observation of Weak Localization of Light in a Random Medium. *Physical Review Letters* **55**, 2692-2695 (1985).

4 Wolf, P. E. & Maret, G. Weak Localization and Coherent Backscattering of Photons in Disordered Media. *Physical Review Letters* **55**, 2696-2699 (1985).

5 Wiersma, D. S., Bartolini, P., Lagendijk, A. & Righini, R. Localization of light in a disordered medium. *Nature* **390**, 671-673 (1997).

6 Chabanov, A. A., Stoytchev, M. & Genack, A. Z. Statistical signatures of photon localization. *Nature* **404**, 850-853 (2000).

7 Wang, J. & Genack, A. Z. Transport through modes in random media. *Nature* **471**, 345-+ (2011).

8 Cao, H. *et al.* Random laser action in semiconductor powder. *Physical Review Letters* **82**, 2278-2281 (1999).

9 Sapienza, L. *et al.* Cavity quantum electrodynamics with Anderson-localized modes. *Science* **327**, 1352-1355, doi:327/5971/1352 [pii] 10.1126/science.1185080 (2010).

10 Sperling, T., Buhrer, W., Aegerter, C. M. & Maret, G. Direct determination of the transition to localization of light in three dimensions. *Nature Photonics* **7**, 48-52 (2013).

11 Riboli, F. *et al.* Engineering of light confinement in strongly scattering disordered media. *Nature Materials* **13**, 720-725 (2014).

12 Vollrath, F. & Knight, D. P. Liquid crystalline spinning of spider silk. *Nature* **410**, 541-548 (2001).

13 Anderson, P. W. Absence of Diffusion in Certain Random Lattices. *Phys Rev* **109**, 1492-1505 (1958).

14 Liu, J. *et al.* Random nanolasing in the Anderson localized regime. *Nat Nanotechnol* **9**, 285-289, doi:Doi 10.1038/Nnano.2014.34 (2014).

15 Vollhardt, D. & Wolfle, P. Diagrammatic, Self-Consistent Treatment of the Anderson Localization Problem in d $\leq$ 2 Dimensions. *Physical Review B* **22**, 4666-4679 (1980).

16 Schwartz, T., Bartal, G., Fishman, S. & Segev, M. Transport and Anderson localization in disordered two-dimensional photonic lattices. *Nature* **446**, 52-55 (2007).
17 Vynck, K., Burresi, M., Riboli, F. & Wiersma, D. S. Photon management in two-dimensional disordered media. *Nature Materials* **11**, 1017-1022 (2012).
18 Busch, K., Soukoulis, C. M. & Economou, E. N. Transport and Scattering Mean Free Paths of Classical Waves. *Physical Review B* **50**, 93-98 (1994).
19 Andreasen, J. *et al.* Modes of random lasers. *Advances in Optics and Photonics* **3**, 88-127 (2011).
20 Jabbari, E., Kim, D. H., Lee, L. P., Ghaemmaghami, A. & Khademhosseini, A. *Handbook of Biomimetics and Bioinspiration Biologically-Driven Engineering of Materials, Processes, Devices, and Systems*. (World Scientific Publishing Company, 2014).
21 Parker, S. T. *et al.* Biocompatible Silk Printed Optical Waveguides. *Advanced Materials* **21**, 2411-2415 (2009).
22 Shi, Z., Wang, J. & Genack, A. Z. Microwave conductance in random waveguides in the cross-over to Anderson localization and single-parameter scaling. *P Natl Acad Sci USA* **111**, 2926-2930 (2014).
23 Strudley, T., Zehender, T., Blejean, C., Bakkers, E. P. A. M. & Muskens, O. L. Mesoscopic light transport by very strong collective multiple scattering in nanowire mats. *Nature Photonics* **7**, 413-418 (2013).
24 Mascheck, M. *et al.* Observing the localization of light in space and time by ultrafast second-harmonic microscopy. *Nature Photonics* **6**, 293-298 (2012).
25 Holik, H. in *Handbook of Paper and Board* (Wiley-VCH 2013).
26 Nieuwenhuizen, T. M. & Vanrossum, M. C. W. Intensity Distributions of Waves Transmitted through a Multiple Scattering Medium. *Physical Review Letters* **74**, 2674-2677 (1995).
27 Davy, M., Shi, Z., Wang, J. & Genack, A. Z. Transmission statistics and focusing in single disordered samples. *Optics Express* **21**, 10367-10375 (2013).
28 van Rossum, M. C. W. & Nieuwenhuizen, T. M. Multiple scattering of classical waves: microscopy, mesoscopy, and diffusion. *Reviews of Modern Physics* **71**, 313-371 (1999).
29 Jiang, X. Y. & Soukoulis, C. M. Localized random lasing modes and a path for observing localization. *Physical Review E* **65**, 025601(R) (2002).
30 Stano, P. & Jacquod, P. Suppression of interactions in multimode random lasers in the Anderson localized regime. *Nature Photonics* **7**, 66-71 (2013).
31 Apalkov, V. M. & Raikh, M. E. Universal fluctuations of the random lasing threshold in a sample of a finite area. *Physical Review B* **71**, 054203 (2005).
32 Hennessy, K. *et al.* Quantum nature of a strongly coupled single quantum dot-cavity system. *Nature* **445**, 896-899 (2007).
33 Kaur, J. *et al.* Photoprotection by Silk Cocoons. *Biomacromolecules* **14**, 3660-3667 (2013).

34 Lee, S. M. *et al.* Greatly Increased Toughness of Infiltrated Spider Silk. *Science* **324**, 488-492 (2009).

35 Choi, S. H. & Kim, Y. L. Random lasing mode alterations by single-nanoparticle perturbations. *Appl Phys Lett* **100**, 041101 (2012).

36 Popoff, S. M. *et al.* Measuring the transmission matrix in optics: an approach to the study and control of light propagation in disordered media. *Physical Review Letters* **104**, 100601 (2010).

37 Kim, M. *et al.* Maximal energy transport through disordered media with the implementation of transmission eigenchannels. *Nature Photonics* **6**, 581-585, doi:http://www.nature.com/nphoton/journal/v6/n9/abs/nphoton.2012.159.html#supplementary-information (2012).

38 Park, J. H. *et al.* Reeling of recombinant flourescence cocoons through low temperature decompressed cooking. *Journal of Sericultural and Entomological Science* **51**, 142-146 (2013).

39 Song, Q. *et al.* Random lasing in bone tissue. *Optics Letters* **35**, 1425-1427 (2010).

40 Choi, S. H. & Kim, Y. L. Hybridized/coupled multiple resonances in nacre. *Physical Review B* **89**, 035115 (2014).

41 Press, W. H., Flannery, B. P., Teukolsky, S. A. & Vetterling, W. T. (Cambridge University Press, 2007).

42 Choi, S. H. Fast and robust extraction of optical and morphological properties of human skin using a hybrid stochastic-deterministic algorithm: Monte-Carlo simulation study. *Laser Med Sci* **25**, 733-741 (2010).

43 Drummy, L. F. *et al.* Low Voltage Electron Microscopy of Silk Fibers and Films. *Microscopy and Microanalysis* **11**, 1268-1269, doi:doi:10.1017/S1431927605505622 (2005).

44 Hakimi, O., Knight, D. P., Knight, M. M., Grahn, M. F. & Vadgama, P. Ultrastructure of insect and spider cocoon silks. *Biomacromolecules* **7**, 2901-2908 (2006).

45 Trancik, J. E., Czernuszka, J. T., Bell, F. I. & Viney, C. Nanostructural features of a spider dragline silk as revealed by electron and X-ray diffraction studies. *Polymer* **47**, 5633-5642 (2006).

46 Shcherbo, D. *et al.* Far-red fluorescent tags for protein imaging in living tissues. *Biochem J* **418**, 567-574 (2009).

47 Tamura, T. *et al.* Germline transformation of the silkworm Bombyx mori L-using a piggyBac transposon-derived vector. *Nature Biotechnology* **18**, 81-84 (2000).

48 Teule, F. *et al.* Silkworms transformed with chimeric silkworm/spider silk genes spin composite silk fibers with improved mechanical properties. *Proceedings of the National Academy of Sciences of the United States of America* **109**, 923-928 (2012).

49 Iizuka, T. *et al.* Colored Fluorescent Silk Made by Transgenic Silkworms. *Adv Funct Mater* **23**, 5232-5239 (2013).

50 Kim, D. W. *et al.* Novel fabrication of fluorescent silk utilized in biotechnological and medical applications. *Biomaterials* **70**, 48-56 (2015).

51 Kim, S. W. *et al.* Utilization of the Bombyx mori heat shock protein 70 promoter for screening transgenic silkworms. *Entomol Res* **43**, 282-287 (2013).

52 Milner, V. & Genack, A. Z. Photon localization laser: Low-threshold lasing in a random amplifying layered medium via wave localization. *Physical Review Letters* **94**, 073901, doi:Artn 073901
Doi 10.1103/Physrevlett.94.073901 (2005).

53 Pena, A., Girschik, A., Libisch, F., Rotter, S. & Chabanov, A. A. The single-channel regime of transport through random media. *Nat Commun* **5**, 3488 (2014).

54 Choi, S. H., Byun, K. M. & Kim, Y. L. Excitation of multiple resonances in 1D Anderson localized systems for efficient light amplification. *Opt Lett* **40**, 847-850, doi:Doi 10.1364/Ol.40.000847 (2015).

55 Dorokhov, O. N. On the Coexistence of Localized and Extended Electronic States in the Metallic Phase. *Solid State Commun* **51**, 381-384 (1984).

56 Shi, Z. & Genack, A. Z. Transmission Eigenvalues and the Bare Conductance in the Crossover to Anderson Localization. *Physical Review Letters* **108**, 043901 (2012).

57 Lenke, R. & Maret, G. in *Scattering in Polymeric and Colloidal Systems* (eds W. Brown & K. Mortensen) (CRC Press 2000).

58 Conley, G. M., Burresi, M., Pratesi, F., Vynck, K. & Wiersma, D. S. Light Transport and Localization in Two-Dimensional Correlated Disorder. *Physical Review Letters* **112**, 143901 (2014).

59 Kim, Y. L. *et al.* Low-coherence enhanced backscattering: Review of principles and applications for colon cancer screening. *Journal of Biomedical Optics* **11**, 041125 (2006).

60 Liu, J., Xu, Z., Song, Q., Konger, R. L. & Kim, Y. L. Enhancement factor in low-coherence enhanced backscattering and its applications for characterizing experimental skin carcinogenesis. *Journal of Biomedical Optics* **15**, 037011 (2010).

61 Ntziachristos, V. Going deeper than microscopy: the optical imaging frontier in biology. *Nature Methods* **7**, 603-614 (2010).

62 Onufrak, M. A. V., Konger, R. L. & Kim, Y. L. Telecentric suppression of diffuse light in imaging of highly anisotropic scattering media. *Optics Letters* **41**, 143-146 (2016).

63 Prahl, S. A., van Gemert, M. J. C. & Welch, A. J. Determining the Optical Properties of Turbid Media by Using the Adding Doubling Method. *Applied Optics* **32**, 559-568 (1993).

64 Henyey, L. G. & Greenstein, J. L. Diffuse radiation in the galaxy. *Astrophys J* **93**, 70-83 (1941).

65 Garcia, P. D., Sapienza, R. & Lopez, C. Photonic Glasses: A Step Beyond White Paint. *Advanced Materials* **22**, 12-19 (2010).

66 Levi, L. *et al.* Disorder-enhanced transport in photonic quasicrystals. *Science* **332**, 1541-1544, doi:10.1126/science.1202977 (2011).

67 Pradhan, P. & Kumar, N. Localization of Light in Coherently Amplifying Random-Media. *Physical Review B* **50**, 9644-9647 (1994).

68 Lawandy, N. M., Balachandran, R. M., Gomes, A. S. L. & Sauvain, E. Laser Action in Strongly Scattering Media. *Nature* **368**, 436-438 (1994).

69 Polson, R. C., Chipouline, A. & Vardeny, Z. V. Random lasing in pi-conjugated films and infiltrated opals. *Advanced Materials* **13**, 760-764 (2001).

70 Wiersma, D. S. The physics and applications of random lasers. *Nat Phys* **4**, 359-367, doi:Doi 10.1038/Nphys971 (2008).

71 Leong, E. S. P. & Yu, S. F. UV random lasing action in p-SiC(4H)/i-ZnO-SiO2 nanocomposite/n-ZnO : Al heterojunction diodes. *Advanced Materials* **18**, 1685-1688 (2006).

72 Zhu, H. *et al.* Low-Threshold Electrically Pumped Random Lasers. *Advanced Materials* **22**, 1877-1881 (2010).

73 Chu, S. *et al.* Electrically pumped waveguide lasing from ZnO nanowires. *Nature Nanotechnology* **6**, 506-510 (2011).

74 Pendry, J. B. Quasi-Extended Electron-States in Strongly Disordered-Systems. *J Phys C Solid State* **20**, 733-742 (1987).

75 Tartakovskii, A. V., Fistul, M. V., Raikh, M. E. & Ruzin, I. M. Hopping Conductivity of Metal-Semiconductor Metal Contacts. *Sov Phys Semicond+* **21**, 370-373 (1987).

76 Bertolotti, J., Gottardo, S., Wiersma, D. S., Ghulinyan, M. & Pavesi, L. Optical necklace states in Anderson localized 1D systems. *Phys Rev Lett* **94**, 113903 (2005).

77 Sebbah, P., Hu, B., Klosner, J. M. & Genack, A. Z. Extended quasimodes within nominally localized random waveguides. *Physical Review Letters* **96**, 183902 (2006).

78 Bliokh, K. Y., Bliokh, Y. P., Freilikher, V., Genack, A. Z. & Sebbah, P. Coupling and level repulsion in the localized regime: From isolated to quasiextended modes. *Physical Review Letters* **101**, 133901 (2008).

79 Labonte, L., Vanneste, C. & Sebbah, P. Localized mode hybridization by fine tuning of two-dimensional random media. *Opt Lett* **37**, 1946-1948 (2012).

80 Chen, L. & Jiang, X. Y. Characterization of short necklace states in the logarithmic transmission spectra of localized systems. *Journal of Physics: Condensed Matter* **25**, 175901 (2013).

81 Fritz, M. *et al.* Flat Pearls from Biofabrication of Organized Composites on Inorganic Substrates. *Nature* **371**, 49-51 (1994).

82 Gao, H. J., Ji, B. H., Jager, I. L., Arzt, E. & Fratzl, P. Materials become insensitive to flaws at nanoscale: Lessons from nature. *Proceedings of the National Academy of Sciences of the United States of America* **100**, 5597-5600 (2003).

83 Li, X. D., Chang, W. C., Chao, Y. J., Wang, R. Z. & Chang, M. Nanoscale structural and mechanical characterization of a natural nanocomposite material: The shell of red abalone. *Nano Letters* **4**, 613-617 (2004).

84 Espinosa, H. D. *et al.* Tablet-level origin of toughening in abalone shells and translation to synthetic composite materials. *Nature Communications* **2**, 173, doi:10.1038/ncomms1172 (2011).

85 Li, Y. Q., Yu, T., Yang, T. Y., Zheng, L. X. & Liao, K. Bio-Inspired Nacre-like Composite Films Based on Graphene with Superior Mechanical, Electrical, and Biocompatible Properties. *Advanced Materials* **24**, 3426-3431 (2012).

86 Li, X. Q. & Zeng, H. C. Calcium Carbonate Nanotablets: Bridging Artificial to Natural Nacre. *Advanced Materials* **24**, 6277-6282 (2012).

87 Podsiadlo, P. *et al.* Ultrastrong and stiff layered polymer nanocomposites. *Science* **318**, 80-83, doi:DOI 10.1126/science.1143176 (2007).

88 Tang, Z. Y., Kotov, N. A., Magonov, S. & Ozturk, B. Nanostructured artificial nacre. *Nature Materials* **2**, 413-U418, doi:Doi 10.1038/Nmat906 (2003).

89 Munch, E. *et al.* Tough, bio-inspired hybrid materials. *Science* **322**, 1516-1520, doi:322/5907/1516 [pii]
10.1126/science.1164865 (2008).

90 Tan, T. L., Wong, D. & Lee, P. Iridescence of a shell of mollusk Haliotis Glabra. *Optics Express* **12**, 4847-4854 (2004).

91 Brink, D. J. & van der Berg, N. G. An investigation of green iridescence on the mollusc Patella granatina. *Journal of Physics D-Applied Physics* **38**, 338-343 (2005).

92 Finnemore, A. *et al.* Biomimetic layer-by-layer assembly of artificial nacre. *Nature Communications* **3**, 966, doi:10.1038/ncomms1970 (2012).

93 Snow, M. R., Pring, A., Self, P., Losic, D. & Shapter, J. The origin of the color of pearls in iridescence from nano-composite structures of the nacre. *Am Mineral* **89**, 1353-1358 (2004).

94 Li, B. *et al.* One-dimensional photonic bandgap structure in abalone shell. *Chinese Sci Bull* **50**, 1529-1531 (2005).

95 Vukusic, P. & Sambles, J. R. Photonic structures in biology. *Nature* **424**, 852-855 (2003).

96 Xu, Z. *et al.* Spectroscopic visualization of nanoscale deformation in bone: interaction of light with partially disordered nanostructure. *Journal of Biomedical Optics* **15**, 060503 (2010).

97 Choi, S. H., Kim, Y. L. & Byun, K. M. Graphene-on-silver substrates for sensitive surface plasmon resonance imaging biosensors. *Optics Express* **19**, 458-466 (2010).

98 Jiang, X. Y. & Soukoulis, C. M. Time dependent theory for random lasers. *Physical Review Letters* **85**, 70-73 (2000).

99 Andreasen, J., Vanneste, C., Ge, L. & Cao, H. Effects of spatially nonuniform gain on lasing modes in weakly scattering random systems. *Physical Review A* **81**, 043818 (2010).

100 Ghosh, G. Dispersion-equation coefficients for the refractive index and birefringence of calcite and quartz crystals. *Optics Communications* **163**, 95-102 (1999).

101 El-Kashef, H. The necessary requirements imposed on polar dielectric laser dye solvents. *Physica B* **279**, 295-301 (2000).

102 Leupacher, W. & Penzkofer, A. Refractive-Index Measurement of Absorbing Condensed Media. *Applied Optics* **23**, 1554-1558 (1984).
103 Milner, V. & Genack, A. Z. Photon localization laser: Low-threshold lasing in a random amplifying layered medium via wave localization. *Physical Review Letters* **94**, 07390, doi:Artn 073901
Doi 10.1103/Physrevlett.94.073901 (2005).
104 Song, Q., Xiao, S., Xu, Z., Shalaev, V. M. & Kim, Y. L. Random laser spectroscopy for nanoscale perturbation sensing. *Optics Letters* **35**, 2624-2626 (2010).
105 Tureci, H. E., Ge, L., Rotter, S. & Stone, A. D. Strong interactions in multimode random lasers. *Science* **320**, 643-646, doi:DOI 10.1126/science.1155311 (2008).
106 Choi, S. H., Kwak, B., Han, B. & Kim, Y. L. Competition between excitation and emission enhancements of quantum dots on disordered plasmonic nanostructures. *Optics Express* **20**, 16785-16793 (2012).
107 Cao, H., Jiang, X. Y., Ling, Y., Xu, J. Y. & Soukoulis, C. M. Mode repulsion and mode coupling in random lasers. *Physical Review B* **67**, 161101(R) (2003).
108 van der Molen, K. L., Tjerkstra, R. W., Mosk, A. P. & Lagendijk, A. Spatial extent of random laser modes. *Physical Review Letters* **98**, 143901, doi:Artn 143901
Doi 10.1103/Physrevlett.98.143901 (2007).
109 Barnes, M. D., Whitten, W. B., Arnold, S. & Ramsey, J. M. Homogeneous Linewidths of Rhodamine-6g at Room-Temperature from Cavity-Enhanced Spontaneous Emission Rates. *J Chem Phys* **97**, 7842-7845 (1992).
110 Leonetti, M., Conti, C. & Lopez, C. The mode-locking transition of random lasers. *Nature Photonics* **5**, 615-617 (2011).
111 Yeh, P. *Optical Waves in Layered Media*. (Wiley, 1988).
112 Pendry, J. B. Symmetry and Transport of Waves in One-Dimensional Disordered-Systems. *Adv Phys* **43**, 461-542 (1994).
113 Hecht, E. *Optics*. 4 edn, (Addison-Wesley, 2001).

VITA

VITA

Education

Ph.D. in Weldon School of Biomedical Engineering, Purdue University, 2016.5

M.S. in Interdisciplinary Program of Bioengineering, Seoul National University, 2009.2

B.S. in Biomedical Engineering, Yonsei University, 2006.8

Professional Recognitions, Awards, and Honors

2015.3 Bilsland Dissertation Fellowship: to outstanding PhD candidates in their final year of doctoral degree completion, Purdue University, West Lafayette, IN

2011.8 Abbott Laboratories Research Fellowship, Purdue University, West Lafayette, IN

2010.8 Ross Fellowship, Purdue University, West Lafayette, IN

2006.8 Highest Distinction and Fellowship, Yonsei University, Wonju, South Korea

2006.2 High Distinction and Fellowship, Yonsei University, Wonju, South Korea

2005.8 Highest Distinction and Fellowship, Yonsei University, Wonju, South Korea

Referee Activities

Referee for Optics Letters, Optics Express, Applied Physics Letters, AIP Advances, and Journal of Applied Physics (Refereed about 40 manuscripts)

Research Interests

Light localization and Random lasing in natural/synthesized materials; Surface plasmon resonance; Theories and computations in electrodynamics; Nano/micro- structure fabrication; Molecular dynamics; Quantitative modeling of biophysical phenomena; Coherent backscattering of light; Inverse algorithm for spectrum analysis

Skills

Optical System Build-up: Transmission matrix measurement system, High Resolution Spectrograph and Hyper-Spectrograph imaging System for Random Lasing Experiment, Coherent Backscattering, Surface Plasmon Resonance, Visible Reflectance Spectroscopy, and Random laser integrated microfluidics system

Mathematical Analysis/Simulation and its Programming from scratch: Ab-initio method for the electronic structure using Hartree-Fock Theory and Kohn-Sham Density Functional Theory; Numerically solving Partial Differential Equation using Finite Element Method, Finite Difference Method, Finite Volume Method and Finite Difference Time Domain method; Optimization Algorithm (Genetic Algorithm and Deterministic Searching Methods); Monte-Carlo Method for photon transport

Nano/micro- Structure Fabrication: UV Photo Lithography (MA6-II)

Ultramicroscope Imaging: Scanning Electron Microscope (Hitachi S-4800 and JEOL6400) and Confocal Microscope (Olympus FV1000 Laser Scanning Confocal Microscope)

Digital and Analog Electric Circuit Design

PUBLICATIONS

PUBLICATIONS

Peer-reviewed Journal Publications

20. Taehoon Kim, **Seung Ho Choi**, Nathan Lambert-Cheatham, Janice E. Kritchevsky, and Young L. Kim, “Spectrometer-free imaging for quantitative hemoglobin sensing and anemia diagnosis in animals”, in preparation.

19. Jung Woo Leem, **Seung Ho Choi***, Kwang-Ho Choi, and Young L. Kim (* Equal contribution), “Wholly integrated plasmonic fabrics: A biogenic approach”, in preparation.

18. Soocheol Kim, Sung Yeun Yang, **Seung Ho Choi**, Young L. Kim, Won Hyoung Ryu, and Chulmin Joo, “Random lasing on the directionality of nanofibers in silk fibroin scaffolds”, in preparation.

17. **Seung Ho Choi**, Siddhant Jaitpal, John Rauchenstein, Pan Chae Kim, Kyung Min Byun, and Young L. Kim, “Native pearls: efficient and steady lasing nanoarchitecture on evolutionary optimum”, in preparation.

16. **Seung Ho Choi**, Seong-Wan Kim, Michelle A. Visbal Onufrak, Seong-Ryul Kim, Kwang-Ho Choi, Hakseok Ko, Wonshik Choi, Tae-Won Goo, and Young L. Kim, “Light in natural silk: biogenic localization proximal to the Anderson regime”, in preparation, 2016.

15. Zhuoxian Wang, Xiangeng Meng, **Seung Ho Choi**, Sebastian Knitter, Young L. Kim, Hui Cao, Vladimir M. Shalaev, and Alexandra Boltasseva, “Controlling random lasing with 3-D plasmonic nanorod metamaterials”, Nano Letters, in press, 2016.

14. **Seung Ho Choi**, Kyung Min Byun, and Young L. Kim, “Excitation of multiple resonances in 1D Anderson localized systems for efficient light amplification”, Optics Letters, vol. 40, pp. 847-850, 2015.

13. **Seung Ho Choi** and Young L. Kim, “The potential of naturally occurring lasing for biological and chemical sensors”, Biomedical Engineering Letters, vol. 4, pp. 201-212, 2014.

12. **Seung Ho Choi** and Young L. Kim, “Hybridized/coupled multiple resonances in nacre”, Physical Review B, vol. 89, pp. 035115, 2014.

11. Nak-Hyeon Kim, Kyung Min Byun, **Seung Ho Choi**, and Young L. Kim, “Improvement of plasmonic field-matter interaction by subwavelength dielectric gratings”, Applied Physics B, vol. 13, pp. 5522-2, 2013.

10. **Seung Ho Choi**, Bongseop Kwak, Bumsoo Han, and Young L. Kim, “Competition between excitation and emission enhancement of quantum dots on disordered plasmonic nanostructures”, Optics Express, vol. 20, pp. 16785-16793, 2012.

9. **Seung Ho Choi** and Young L. Kim, “Random lasing mode alterations by single-nanoparticle perturbations”, Applied Physics Letters, vol. 100, pp. 041101-041104, 2012. (Cover Article)

8. Seong Min Jang, Donghyun Kim, **Seung Ho Choi**, Kyung Min Byun, and Sung June Kim, “Enhancement of localized surface plasmon resonance detection by incorporating metal-dielectric double-layered subwavelength gratings”, Applied Optics, vol. 50(18), pp. 2846-2854, 2011.

7. **Seung Ho Choi**, Sung June Kim, Chang-Hwan Im, Shin Ae Kim, and Daejoong Kim, "Quantitative model for the change of optical resonance in neural activity detection systems based on surface plasmon resonance", Optics & Laser Technology, vol. 43, pp. 938-948, 2011.

6. **Seung Ho Choi**, Young L. Kim, and Kyung Min Byun, "Graphene-on-silver substrates for sensitive surface plasmon resonance imaging biosensors", Optics Express, vol. 19(2), pp. 458-466, 2011.

5. Qinghai Song, Zhengbin Xu, **Seung Ho Choi**, Xuanhao Sun, Shumin Xiao, O Akkus, and Young L. Kim, "Detection of nanoscale structural changes in bone using random lasers", Biomedical Optics Express, vol. 1(5), pp. 1401-1407, 2010.

4. **Seung Ho Choi** and Kyung Min Byun, “Investigation on an application of silver substrates for a sensitive surface plasmon resonance imaging detection”, Journal of Optical Society of America A, vol. 27, pp. 2229-2236, 2010.

3. **Seung Ho Choi**, “Fast and robust extraction of human skin optical and morphological properties using hybrid stochastic-deterministic algorithm: Monte-carlo simulation study”, Lasers in Medical Science, vol. 25, pp. 733-741, 2010.

2. **Seung Ho Choi**, Sung June Kim, and Kyung Min Byun, “Characteristics of light emission from surface plasmons based on silver diffraction gratings”, Optics Communications, vol. 283, pp. 2961-2966, 2010.

1. **Seung Ho Choi**, Sung June Kim, and Kyung Min Byun, “Design study for transmission improvement of resonant surface plasmons using dielectric diffraction gratings”, Applied Optics, vol. 48, pp. 2924-2931, 2009.

Conference Publications

12. Jung Woo Leem, **Seung Ho Choi**, Kwang-Ho Choi, and Young L. Kim, “Wholly integrated plasmonic fabrics”, 2016 US-Korea Conference on Science, Technology and Entrepreneurship, Dallas, TX, August 10, 2016.

11. **Seung Ho Choi**, Jung Woo Leem, Kwang-Ho Choi, and Young L. Kim, “Biogenic light trapping in natural fibers toward scalable photocatalysis”, 2016 Collaborative Conference on 3D and Materials Research, South Korea, June 20, 2016.

10. **Seung Ho Choi** and Young L. Kim, “Biogenic Anderson light localization”, Inaugural Workshop for Purdue Quantum Center, West Lafayette, IN, USA, October 14, 2015.

9. Zhuoxian Wang, Xiangeng Meng, **Seung Ho Choi**, Young L. Kim, Vladimir M. Shalaev, and Alexandra Boltasseva, “Plasmonic random lasing in strongly scattering regime with slanted silver nanorod array”, CLEO Laser Science to Photonic Applications, San Jose, CA, USA, May 12-14, 2015.

8. **Seung Ho Choi** and Young L. Kim, “Natural production of biological optical systems”, SPIE Photonics West, San Francisco, CA, USA, February 1-6, 2015.

7. **Seung Ho Choi** and Young L. Kim, “Self-formed ultraefficient resonators from mollusk shells”, SPIE Photonics West, San Francisco, CA, USA, February 1-6, 2014.

6. **Seung Ho Choi**, Zhengbin Xu, and Young L. Kim, “From random lasing to ultrasensitive spectroscopy”, BIOMED, Miami, FL, USA, April 29-May 2, 2012.

5. **Seung Ho Choi** and Young L. Kim, “Lasing modes in disordered media for single-nanoparticle quantitation: a new approach for biosensing”, SPIE Photonics West, San Francisco, CA, USA, January 21-26, 2012.

4. Seong Min Jang, Donghyun Kim, **Seung Ho Choi**, Sung June Kim, and Kyung Min Byun, “Enhanced localized surface plasmon resonance detection based on metal-dielectric double-layered nanowires”, The Korean Society of Medical & Biological Engineering Annual Meeting, Seoul, Korea, November 13, 2009.

3. **Seung Ho Choi** and Sung June Kim, “Development of geometry-based finite element model for subretinal electrical stimulation”, The Korean Society of Medical & Biological Engineering Annual Meeting, Seoul, Korea, November 9, 2007.

2. Eui Tae Kim, **Seung Ho Choi**, and Sung June Kim, “3-D pillar structured retinal electrode array of local point-of-stimulation technology for emerging higher resolution information transmission”, The Korean Society of Medical & Biological Engineering Annual Meeting, Seoul, Korea, November 9, 2007.

1. **Seung Ho Choi**, Chang-Hwan Im, and Byungjo Jung, “Improvement of fitting method for visible reflectance spectrum to extract skin optical properties”, Optical Society of Korea Annual Meeting, Kwangju, Korea, February 8-9, 2007.

Conference Oral-Presentations

2. **Seung Ho Choi** and Young L. Kim, “Lasing modes in disordered media for single-nanoparticle quantitation: a new approach for biosensing”, SPIE Photonics West, San Francisco, CA, USA, January 21, 2012.

1. **Seung Ho Choi**, Chang-Hwan Im, and Byungjo Jung, “Improvement of fitting method for visible reflectance spectrum to extract skin optical properties”, Optical Society of Korea Annual Meeting, Kwangju, Korea, February 8, 2007.

U.S. and International Patents

1. “Silk-Based Textile Platforms of Semiconductor Photocatalysis Using Light Localization,” US Patent No: CN ZL200780026888.4, issued date: 08/27/2014, inventors: Young L. Kim and **Seung Ho Choi**.